




Joint Inference of Population, Cosmology, and Neutron Star Equation of State from Gravitational Waves of Dark Binary Neutron Stars

Tathagata Ghosh ^{1,*} Bhaskar Biswas ^{2,3} Sukanta Bose ^{4,1} and Shasvath J. Kapadia ¹

¹*Inter-University Centre for Astronomy and Astrophysics, Post Bag 4, Ganeshkhind, Pune 411 007, India*

²*Universität Hamburg, D-22761 Hamburg, Germany*

³*The Oskar Klein Centre, Department of Astronomy, Stockholm University, AlbaNova, SE-10691 Stockholm, Sweden*

⁴*Department of Physics & Astronomy, Washington State University, 1245 Webster, Pullman, WA 99164-2814, USA*

(Dated: July 24, 2024)

Gravitational waves (GWs) from binary neutron stars (BNSs) are expected to be accompanied by electromagnetic (EM) emissions, which help to identify the host galaxy. Since GW events directly measure their luminosity distances, joint GW-EM observations from BNSs help to study cosmology, particularly the Hubble constant, unaffected by cosmic distance ladder systematics. However, detecting EM counterparts from BNS mergers is not always possible. Additionally, the tidal deformations of BNS components offer insights into the neutron star (NS) equation of state (EoS). In such cases, the tidal parameters of NSs, combined with the knowledge of the NS EoS, can break the degeneracy between mass parameters and redshift, allowing for the inference of the Hubble constant. Several efforts have aimed to infer the Hubble constant using the tidal parameters of BNSs, without EM counterparts, termed dark BNSs. Moreover, some studies have focused on the joint estimation of population and NS EoS for unbiased NS EoS estimation. However, none of the works consistently combined the uncertainties of population, cosmology, and NS EoS within a Bayesian framework. In this study, we propose a novel Bayesian analysis to jointly constrain the NS EoS, population, and cosmological parameters using a population of dark BNSs detected through GW observations. This method can constrain the Hubble constant to $H_0 = 67.40^{+68.52}_{-39.25}$ km s⁻¹ Mpc⁻¹ ($H_0 = 75.15^{+37.15}_{-23.88}$ km s⁻¹ Mpc⁻¹) using as few as 5 BNS observations following Gaussian (double Gaussian) mass distribution, detected by Advanced LIGO and Advanced Virgo detectors operating at O5 sensitivity. We also demonstrate the statistical robustness of the method by analyzing 50 BNS events with the same detector network, resulting in $H_0 = 69.81^{+7.12}_{-6.31}$ km s⁻¹ Mpc⁻¹ and $H_0 = 71.21^{+6.67}_{-6.13}$ km s⁻¹ Mpc⁻¹ for the Gaussian and double Gaussian mass distributions, respectively. This level of precision and accuracy is unattainable without incorporating NS EoS, especially when observing BNS mergers without EM counterpart information.

I. INTRODUCTION

In the present era of precision cosmology, one of the primary pursuits remains the precise measurement of the Hubble constant, H_0 – a fundamental observable that quantifies the current expansion rate of the Universe. However, presently, there exists a discrepancy between the measurements of the Hubble constant from two different observations. The direct measurement of $H_0 = 73.04 \pm 1.04$ km s⁻¹ Mpc⁻¹ [1] from the SH0ES Collaboration is at a $\sim 4.4\sigma$ tension with the indirect inference of $H_0 = 67.36 \pm 0.54$ km s⁻¹ Mpc⁻¹ [2] from the Planck measurements of the cosmic microwave background. This discordance in the measurement of the expansion rate of the Universe may either imply new physics beyond the standard model or be a systematic effect owing to unaccounted uncertainties in one or more measurements. However, there is no conclusive consensus regarding the value of the Hubble constant today. So, it is crucial to pursue observations independent of the aforementioned ones that can help resolve this tension in the values of the Hubble constant.

The first detection of gravitational waves (GWs) from

a binary neutron star by LIGO [3] and Virgo [4] detectors, i.e., from GW170817 [5], along with the observations of its electromagnetic (EM) counterparts – across the spectrum [6] – has opened the window to multi-messenger astronomy involving GWs. This *inter alia* allows probing the cosmic expansion of the Universe. The independent measurements of luminosity distance from GW data and the redshift from EM data, both from GW170817, enabled us to measure the Hubble constant to be $H_0 = 70^{+12.0}_{-8.0}$ km s⁻¹ Mpc⁻¹ [7]. However, GW observations today are dominated by binary black hole (BBH) mergers [8], which are not accompanied by EM counterparts. The so-called bright siren approach, which relies on independent measurements of luminosity distance and redshift, cannot be applied to most GW observations. This is primarily because most of these observations include BBH mergers, which typically lack EM counterparts and, therefore, do not provide redshift information. So, alternative methods have been proposed to infer H_0 from GW observations without EM counterparts. These GW sources are referred to as *dark sirens*. These methods are primarily categorized into two approaches. One such method is the *galaxy catalog* method [9–14], which statistically associates the dark sirens with the redshifts of galaxies within the sky localizations of the corresponding GW events, as potential

* tathag@iucaa.in

host galaxies. The other method, known as the *spectral siren* method [15, 16], statistically derives the redshifts of GW events by comparing the source-frame mass spectrum with the observed masses of BBHs, which are redshifted, as explained later in this section. Both methods utilize complementary approaches to statistically infer the redshifts of GW events and, consequently, the Hubble constant.

In a recent study [17], the LVK collaboration applied both the spectral siren and galaxy catalog methods to infer the Hubble constant to be $H_0 = 68_{-6}^{+8}$ km s⁻¹ Mpc⁻¹ and $H_0 = 68_{-8}^{+12}$ km s⁻¹ Mpc⁻¹, respectively, by using 42 BBHs from GWTC-3 [8] as well as the BNS event GW170817. Each method has distinct strengths and weaknesses. The spectral siren method allows for the variation of GW population parameters but does not benefit from the additional constraining power of galaxy redshifts. In contrast, the galaxy catalog method fixes the GW population parameters during the computation of the selection function. This can introduce potential bias in estimating the cosmological parameters if the assumed population model is incorrect. So, there are ongoing efforts [18, 19] to unify these two methods: the galaxy catalog information is utilized to infer H_0 while marginalizing over the population model uncertainties. This approach effectively integrates the advantages of both methods. Furthermore, there is another approach – termed the *cross-correlation* method – that explores the expected clustering between GW sources and galaxies to infer the redshift information and, hence, the Hubble constant [20–26].

Similar to the spectral method applied to the BBH events, prior knowledge of the mass distribution of BNS also allows us to estimate the Hubble constant due to the narrowness of the NS mass spectrum [27, 28]. For BBH events, the GW waveform is modeled as point-particle dynamics. If we focus only on point-particle dynamics, the source-frame masses m are degenerate with the redshift z , resulting in the measurement of the redshifted masses, $m^z \equiv m(1+z)$, and the luminosity distance by the GW observations. Consequently, all the observables in the GW waveform are invariant under appropriate transformation by $(1+z)$. Unlike the black holes in binary mergers, neutron stars in BNSs are tidally deformed due to the presence of matter. This tidal deformation, which affects the GW phase evolution, depends on the source-frame masses. So, the measurement of tidal deformabilities from the GW signal helps to break the mass-redshift degeneracy, which was first proposed in Ref. [29]. Thus, the measurement of tidal deformabilities can constrain the distance-redshift relation and, hence, cosmological parameters, even in the absence of EM counterpart detections.

Several efforts [30–33] have been spawned by this idea of using BNS tidal deformabilities in GWs to measure the Hubble constant. In Refs. [30, 33], the authors assume that the equation of state (EoS) is known exactly, which is an over-simplification even for the future generation

detector era. On the other hand, Refs. [31, 32] allow for uncertainties in the neutron star EoS while inferring the Hubble constant in the future-generation detector era. Specifically, in Ref. [31], the BNS mass distribution is assumed to be uniform. Consequently, while the maximum mass is inferred from the constrained NS EoS, the minimum mass remains fixed. The choice of the mass model limits the scope of the study to inferring other mass model parameters, which are not explicitly dependent on the NS EoS. However, none of these works [30–33] deduces the population model (including both mass and redshift distributions) of the underlying distribution of GW events. Notably, inferring the mass distribution in conjunction with the NS EoS is essential to mitigating bias in the mass distribution parameters [34, 35] and further constraining the NS EoS.

This paper demonstrates the simultaneous inference of mass distribution, redshift distribution, NS EoS, and cosmological parameters from a population of BNSs hierarchically. Specifically, we unify all the hyperparameters of the models, including the NS EoS model, mass distribution, redshift distribution, and cosmology in the Bayesian Framework. This method becomes promising in the future for several reasons. Firstly, this method does not rely on the availability of EM data. We can expect several BNS detections due to the improved sensitivity of future GW detectors. However, it is not certain that the corresponding EM counterparts can be detected for various reasons, such as BNS events being at large distances or not being in the field of view of EM detectors, etc. Moreover, this methodology can infer the population model, cosmological parameters, and NS EoS solely from GW data – even while employing uniform priors for EoS model parameters. This is a significant improvement in comparison to earlier attempts [30–33], where some knowledge (or even precise knowledge, in some cases) of the EoS was assumed.

The paper is organized as follows. Sec. II elaborates on the methodology used for inferring the population model, cosmological parameters, and EoS model. In Sec. III, different parameterized models corresponding to NS EoS, mass, and redshift distribution are introduced. In Sec. IV, we discuss the simulation performed in this work to show the efficacy of the proposed methodology. The results are presented in Sec. V. We conclude this paper with a discussion on the implications of these results for future GW detectors and nuclear experiments.

II. METHODOLOGY

In this section, we briefly describe the Bayesian inference for the joint estimation of NS EoS, along with their underlying mass distribution, redshift distribution, and cosmological parameters using GW data from a population of BNS. The set of hyperparameters $\Lambda = \{\Lambda_{\mathcal{E}}, \Lambda_m, \Lambda_z, \Lambda_c\}$ involved in this work corresponds to different parameterized models that describe NS EoS,

BNS mass distribution, redshift evolution, and cosmology, respectively¹. We also compare the estimates of population and cosmological parameters with and without incorporating NS EoS to highlight its impact on constraining these parameters. The method without NS EoS, essentially the spectral siren method, involves the set of hyperparameters $\mathbf{\Lambda} = \{\mathbf{\Lambda}_m, \mathbf{\Lambda}_z, \mathbf{\Lambda}_c\}$. However, the Bayesian framework, a generic approach, remains the same, regardless of whether the NS EoS parameters are employed. We refer to these hyperparameters as model parameters for the rest of the paper. In order to constrain the model parameters, one needs first to perform Bayesian parameter estimation of the BNS source parameters of all such detected events individually. The posteriors of the source parameters, once obtained, would be utilized to infer joint posterior distributions of the model hyperparameters, as follows:

$$p(\mathbf{\Lambda} | \{d\}) \propto p(\mathbf{\Lambda}) \prod_{i=1}^N \frac{1}{\beta(\mathbf{\Lambda})} \int \mathcal{L}(d_i | \boldsymbol{\theta}_i) p(\boldsymbol{\theta}_i | \mathbf{\Lambda}) d\boldsymbol{\theta}_i. \quad (1)$$

A brief review of the Bayesian formalism used in this paper is given in Appendix A. In this work, we are concerned with the source-frame BNS masses $m_{1,2}$, their common redshift z , and their corresponding tidal deformabilities $\Lambda_{1,2}$ (not to be confused with any of the model parameters $\mathbf{\Lambda}$, written in boldface) all of which define the set of source parameters, $\boldsymbol{\theta} = \{m_1, m_2, z, \Lambda_1, \Lambda_2\}$, used in Eq. (1). Here, the likelihood $\mathcal{L}(d_i | \boldsymbol{\theta}_i)$ of the individual event is constructed by marginalizing over all BNS parameters except $\{m_1, m_2, z, \Lambda_1, \Lambda_2\}$.² It is also important to note that the individual source parameters obtained from GW observations are not estimated in the source-frame. Instead, they are obtained in the detector-frame and are denoted by $\boldsymbol{\theta}_d = \{\mathcal{M}^z, q, d_L, \Lambda_1, \Lambda_2\}$, where $\mathcal{M}^z = \mathcal{M}(1+z)$ is the detector-frame chirp mass, $q = m_2/m_1$ is the mass ratio and $d_L(z, H_0)$ is the luminosity distance. The model parameters involved in this work are relevant to source-frame parameters $\boldsymbol{\theta}$. So, the posterior samples and the corresponding priors used to estimate the source parameters need to be converted from the detector-frame to the source-frame. Now, the source-frame posterior distributions should be divided by the equivalent source-frame priors $p_{\text{PE}}(\boldsymbol{\theta}_i)$ to construct the semi-marginalized likelihood in the source-frame, as follows:

$$\mathcal{L}(d_i | \boldsymbol{\theta}_i) \propto \frac{p(\boldsymbol{\theta}_i | d_i)}{p_{\text{PE}}(\boldsymbol{\theta}_i)}. \quad (2)$$

Here, the source-frame priors $p_{\text{PE}}(\boldsymbol{\theta})$ can be obtained by multiplying the determinant of the appropriate Jacobian matrix $J\left(\frac{\boldsymbol{\theta}}{\boldsymbol{\theta}_d}\right)$ with detector-frame priors $p_{\text{PE}}(\boldsymbol{\theta}_d)$

employed in estimating source parameters of individual event:

$$p_{\text{PE}}(\boldsymbol{\theta}) = \left| J\left(\frac{\boldsymbol{\theta}}{\boldsymbol{\theta}_d}\right) \right| \times p_{\text{PE}}(\boldsymbol{\theta}_d). \quad (3)$$

The detailed form of the Jacobian is derived in Appendix B.

In Eq. (1), the likelihood \mathcal{L} assumes that the individual events constitute an unbiased representation of the population. However, GW detectors are more sensitive toward high-mass, nearby, and face-on sources. Consequently, the observed population does not truly follow the astrophysical population. So, the selection function $\beta(\mathbf{\Lambda})$ has been included in Eq. (1) to mitigate this bias in estimating model parameters; it is defined as

$$\beta(\mathbf{\Lambda}) = \int p_{\text{det}}(\boldsymbol{\theta}_i) p(\boldsymbol{\theta}_i | \mathbf{\Lambda}) d\boldsymbol{\theta}_i, \quad (4)$$

where $p_{\text{det}}(\boldsymbol{\theta}_i)$ denotes the probability that an event with source parameters $\boldsymbol{\theta}_i$ is detected. In this work, the selection term $\beta(\mathbf{\Lambda})$ is evaluated via Monte Carlo integration over an ensemble of injected signals, N_{inj} from a fiducial population and cosmological parameters $\mathbf{\Lambda}_0$ and determining the number N_{found} that cross the signal-to-noise (SNR) ratio threshold [36, 37]. The selection function is then computed as follows:

$$\beta(\mathbf{\Lambda}) = \frac{1}{N_{\text{inj}}} \sum_{i=1}^{N_{\text{found}}} \frac{p(\boldsymbol{\theta}_i | \mathbf{\Lambda})}{p(\boldsymbol{\theta}_i | \mathbf{\Lambda}_0)} \quad (5)$$

The details of the BNS population, which is used to calculate the selection effect, are mentioned in Sec. IV.

III. MODELS

Our method has been applied to a set of simulated BNS events. We assume parameterized models of NS EoS, mass-redshift distribution of the sources, and cosmology to simulate them. We briefly discuss each model, along with the true values of the model parameters used to construct the mock GW catalog.

A. EoS Model

In this section, we briefly review the hybrid nuclear+piecewise-polytrope (PP) EoS parameterization, which has been employed in previous studies [38–40] to put joint GW-EM constraints on the NS properties. Since the crust has minimal impact [41, 42] on the macroscopic properties of NS, such as mass, radius, and tidal deformability, the conventional Baym-Pethick-Sutherland (BPS) EoS [43] is employed to model the crust within this framework. The fixed crust is subsequently joined with the

¹ We do not consider spin in this work, as detailed in Sec. IV

² The marginalized BNS parameters are, e.g., the orbit's inclination to the line of sight, right ascension and declination of the source, etc.

core EoS in a thermodynamically consistent manner as described in Ref. [44]. The core EoS is divided into two components:

1. The first component is the EoS around the nuclear saturation density (ρ_0), which can be well represented by the parabolic expansion of energy per nucleon

$$e(\rho, \delta) \approx e_0(\rho) + e_{\text{sym}}(\rho)\delta^2, \quad (6)$$

where $e_0(\rho)$ denotes the energy of symmetric nuclear matter for which the number of protons is equal to the number of neutrons, e_{sym} is the energy of the asymmetric nuclear matter (commonly referred to as “symmetry energy” in literature), and $\delta \equiv \frac{\rho_p - \rho_n}{\rho_p + \rho_n}$ is the measure of asymmetry in the neutron number density ρ_n and the proton number density ρ_p . Around ρ_0 , both energies can be further expanded in a Taylor series:

$$e_0(\rho) = e_0(\rho_0) + \frac{K_0}{2}\chi^2 + \dots, \quad (7)$$

$$e_{\text{sym}}(\rho) = e_{\text{sym}}(\rho_0) + L\chi + \frac{K_{\text{sym}}}{2}\chi^2 \dots, \quad (8)$$

where $\chi \equiv (\rho - \rho_0)/3\rho_0 \ll 1$. We limit the Taylor expansion to the second order in χ since we only utilize this expansion up to $1.25\rho_0$. The lowest order parameters are well constrained by experiments, and therefore, we fix them at their median values, such as $e_0(\rho_0) = -15.9$ MeV, and $\rho_0 = 0.16\text{fm}^{-3}$. Consequently, the free parameters of this nuclear-physics-informed model include curvature of symmetric matter K_0 , nuclear symmetry energy e_{sym} , slope L , and curvature of symmetric energy K_{sym} . A survey based on 53 experimental results performed in 2016 [45] found values of $e_{\text{sym}}(\rho_0) = 31.7 \pm 3.2$ MeV and $L = 58.7 \pm 28.1$ MeV. Using these values as priors, a Bayesian analysis performed in Ref. [38] that combined multiple astrophysical observations (GWs and X-rays) has already provided better constraints on these quantities: $e_{\text{sym}}(\rho_0) = 32.0_{-3.01}^{+3.05}$ MeV and $L = 61.0_{-16.0}^{+17.7}$ MeV.

2. At higher densities, the empirical parametrization starts to break down. Following Ref. [46], for densities above $1.25\rho_0$, we adopt a three-piece piecewise-polytrope parameterization. This approach uses polytropic indices Γ_1 , Γ_2 , and Γ_3 , with fixed transition densities at $10^{14.7}$ g/cm³ and 10^{15} g/cm³, respectively.

Finally, it is crucial to ensure that the parameterized EoS adheres to fundamental physical principles, particularly causality and the requirement for pressure to increase monotonically with density. Additionally, in compliance with the principles of special relativity, the speed

of sound within the NS must not exceed the speed of light.

The injected NS EoS parameters for the simulated BNS events are listed in Table I and the maximum mass corresponding to the injected EoS is $m_{\text{max}} = 2.25 M_\odot$. Instead of explicitly using all these NS EoS parameters, we will generally refer to them as $\mathbf{\Lambda}_\mathcal{E} = \{K_0, e_{\text{sym}}, L, K_{\text{sym}}, \Gamma_1, \Gamma_2, \Gamma_3\}$.

B. Population & Cosmology

In this study, we assume that all NSs originate from a common mass distribution $p(m | \mathbf{\Lambda}_m)$ and form BNSs with random pairing:

$$p(m_1, m_2 | \mathbf{\Lambda}_m) \propto p(m_1 | \mathbf{\Lambda}_m)p(m_2 | \mathbf{\Lambda}_m)\Theta(m_2 > m_1), \quad (9)$$

where Θ is the Heaviside step function that enforces the primary mass m_1 be greater than the secondary mass m_2 . There may be a possibility that each companion of a BNS follows a different mass distribution [35] due to different stellar evolutionary processes prior to collapse [47]. However, we restrict the common mass distribution of the binaries in this work for simplicity.

In this work, we investigate two observationally motivated mass distributions of NSs between minimum mass m_{min} and maximum mass m_{max} , as detailed below. To ensure that the mass distribution has vanishing support outside the interval $[m_{\text{min}}, m_{\text{max}}]$, we multiply the probability density function of mass by $\Theta_m(m_{\text{min}}, m_{\text{max}}) = \Theta(m > m_{\text{min}})\Theta(m < m_{\text{max}})$. We set $m_{\text{min}} = 1M_\odot$, which is consistent with the predicted lower bound of NS mass from plausible supernova formation channels [48, 49]. The maximum mass, $m_{\text{max}} = 2.25M_\odot$, is supported by the injected NS EoS parameters noted in Sec. III A.

1. Gaussian Distribution: This mass distribution is primarily motivated by the Gaussian fit to the mass distribution of Galactic NSs [50–52].

$$p_{\mathcal{N}}(m | m_{\text{min}}, m_{\text{max}}, \mu, \sigma) \propto \mathcal{N}(m | \mu, \sigma) \times \Theta_m(m_{\text{min}}, m_{\text{max}}). \quad (10)$$

The Gaussian distribution characterized by mean μ and standard deviation σ is defined in the range $[m_{\text{min}}, m_{\text{max}}]$. So, the mass hyperparameters corresponding to the Gaussian distribution are $\mathbf{\Lambda}_m = \{m_{\text{min}}, m_{\text{max}}, \mu, \sigma\}$. Following Ref. [52], we set $\mu = 1.33 M_\odot$ and $\sigma = 0.09 M_\odot$ as the injected values of the parameters of the Gaussian mass distribution.

2. Double Gaussian Distribution: In this case, the NS mass distribution is taken to follow a double Gaussian distribution, which is the same as the following

two-component Gaussian distribution [53, 54]:

$$p_{\mathcal{N}\mathcal{N}}(m | \mathbf{\Lambda}_m) \propto [w\mathcal{N}(m | \mu_1, \sigma_1) + (1-w)\mathcal{N}(m | \mu_2, \sigma_2)]\Theta_m(m_{\min}, m_{\max}). \quad (11)$$

Here, $\mathbf{\Lambda}_m = \{m_{\min}, m_{\max}, \mu_1, \sigma_1, \mu_2, \sigma_2, w\}$ corresponds to the mass-distribution hyperparameters, consisting of the mean μ_1 (μ_2), the standard deviation σ_1 (σ_2) and the relative weight of two components w . We consider the mass distribution of BNS to be the double Gaussian with $\mu_1 = 1.34 M_\odot$, $\sigma_1 = 0.07 M_\odot$, $\mu_2 = 1.8 M_\odot$, $\sigma_2 = 0.21 M_\odot$ and $w = 0.65$. This distribution is consistent with the NS mass distribution from pulsar mass measurements [53, 54].

Furthermore, we assume that the BNS mass distribution does not evolve with cosmic time, i.e., it is independent of redshift. This is a reasonable assumption for the low-redshift BNSs, which will be observed by the current-generation ground-based detectors. However, we can relax this assumption for the next-generation detectors, probing large horizon redshift for BNS mergers to study whether the mass distribution of BNS varies across cosmic time.

The redshift distribution of BNS mergers can be written as

$$p(z) \propto \frac{dV_c}{dz} \frac{\mathcal{R}(z)}{1+z}, \quad (12)$$

where V_c is the comoving volume and $\mathcal{R}(z)$ is the source-frame BNS merger rate as a function of redshift. The term $(1+z)$ in the denominator of Eq. (12) is used to convert the source-frame time to the detector-frame time. Considering merger-rate $\mathcal{R}(z)$ to be a power-law i.e., $\mathcal{R}(z) \propto (1+z)^\gamma$, the corresponding redshift distribution [55] of BNSs is

$$p(z | \gamma) \propto \frac{dV_c}{dz} (1+z)^{\gamma-1}. \quad (13)$$

In our work, we set the merger index $\gamma = 0$ for creating the mock BNS catalog. We assume flat Λ CDM cosmology to convert the redshift to luminosity distance by using the following relation:

$$d_L(z) = \frac{c(1+z)}{H_0} \int_0^z \frac{dz'}{\sqrt{\Omega_m(1+z')^3 + (1-\Omega_m)}}. \quad (14)$$

where c and Ω_m correspond to the speed of light and matter density, respectively. For our simulations, we consider Λ CDM cosmology with $H_0 = 70 \text{ km s}^{-1} \text{ Mpc}^{-1}$ and $\Omega_m = 0.3$ as the true cosmology.

IV. SIMULATION

We demonstrate the efficacy of our method with a set of simulated BNS signals in a 3-detectors network, comprising two Advanced LIGO detectors (in Hanford and Livingston) [3] and the Advanced Virgo detector [4], operating at their respective O5 design sensitivities [56]³. We construct a mock GW catalog comprising 50 events uniformly distributed across the sky. We consider those GW sources detected with $\text{SNR } \rho \geq 20$. Applying this SNR threshold, we find that the detected simulations are distributed within $\sim 350 \text{ Mpc}$, a typical range for BNS detection in the O5 era [56]. The models for the NS EoS, BNS population, and cosmology are mentioned in Sec. III, along with the corresponding injected values, which are also summarized in Table I. We ignore the spins of neutron stars in the present work. This is a reasonable approximation considering the low observed spins of BNSs [57, 58]. We simulate the BNS signal for 128 seconds using the waveform model, `IMRPhenomPv2_NRTidal` [59], injected in the colored Gaussian noise corresponding to the three detectors. We perform Bayesian parameter estimation of the simulated GW strain data between 20 Hz and 2048 Hz using the nested sampler `dynesty` [60] implemented in `bilby_pipe` [61]. We use the same waveform model employed for injection to obtain the posterior probability distribution of BNS parameters. We perform parameter estimation over the mass pair, tidal deformabilities, luminosity distance, inclination angle, and sky-position. We fix other parameters (see Table 2 in Ref. [61] for the list of BNS parameters) at the injected values to curtail the computational cost of individual-event parameter estimation. In Appendix C, Fig. 13 presents the marginalized joint posteriors of the detected parameters of a BNS event. These parameters are involved in inferring population, NS EoS, and cosmology.

Once we obtain the posterior samples of all detected individual events, we utilize them to constrain the NS EoS, mass-redshift distribution, and cosmological parameters, following the formalism outlined in Sec. II. We consider uniform priors for all the model hyperparameters to be inferred in this study. The priors of the hyperparameters are mentioned in Table I and Table II. We have already discussed that the BNS parameters inferred in the detector-frame need to be converted to the source-frame to calculate the likelihood in the source-frame. Additionally, we perform integration in the component mass frame in Eq. (1), whereas we have inferred chirp mass and mass ratio from GW strain data assuming uniform priors over the respective parameters. So, we need to convert the inferred detected chirp mass and mass ratio to the detected component masses, followed by the transformation to the source-frame component masses. Moreover, we have to

³ <https://dcc.ligo.org/LIGO-T2000012/public>

Model	Parameters	Units	True Values	Priors
EoS	K_0	MeV	239.7	$U(129, 350)$
	e_{sym}	MeV	32.5	$U(21, 43)$
	L	MeV	69	$U(8, 145)$
	K_{sym}	MeV	-174.6	$U(-560, 251)$
	Γ_1	-	3	$U(0.2, 7.8)$
	Γ_2	-	4	$U(1.2, 6.1)$
	Γ_3	-	3.7	$U(0.2, 8)$
Redshift	γ	-	0	$U(-20, 20)$
Cosmology	H_0	$\text{km s}^{-1} \text{Mpc}^{-1}$	70	$U(10, 200)$
	Ω_m	-	0.3	$U(0, 1)$

TABLE I. Summary of hyperparameters for the EoS, redshift, and cosmological model used in this work. The details of hyperparameters for mass models are provided in Table II.

Mass Model	Parameters	Units	True Values	Priors
Gaussian	μ	M_\odot	1.33	$U(1, m_{\text{max}})$
	σ	M_\odot	0.09	$U(0.005, 0.5)$
Double Gaussian	μ_1	M_\odot	1.34	$U(1, 2)$
	σ_1	M_\odot	0.07	$U(0.005, 0.5)$
	μ_2	M_\odot	1.8	$U(\mu_1, m_{\text{max}})$
	σ_2	M_\odot	0.21	$U(0.005, 0.5)$
	w	-	0.65	$U(0, 1)$

TABLE II. Summary of hyperparameters for 2 different mass models used in this work. m_{max} is chosen between $[1, 3] M_\odot$ when EoS is not considered; otherwise m_{max} is determined from the NS EoS. All mass models are defined within the fixed mass range $[m_{\text{min}}, m_{\text{max}}] = [1, 2.25] M_\odot$.

calculate the respective priors in the component masses, corresponding to the uniform priors over detected chirp mass and mass ratio used during the inference of source parameters. In Appendix B, we show the calculation of the Jacobian, which translates the detector-frame parameters to source-frame parameters in order to calculate the GW likelihood in this work.

We calculate the selection function β for the unbiased estimation of hyperparameters in Eq. (1) by considering 10^6 BNSs, following a uniform mass distribution in the source-frame between $1 - 3 M_\odot$. For each BNS signal, we compute the SNR of the simulated BNS signals in the O5 noise realization and thereby determine the selection function following Eq. (5). We do not consider the impact of the tidal effects in calculating the selection function because the tidal effect starts appearing at the 5 post-Newtonian order and has no significant contribution to the amplitude of the GW signal. We have used the nested sampler `Pymultinest` [62] for performing the Bayesian inference of Eq. (1).

V. RESULTS

In this study, we explore how well the NS population and the cosmological parameters can be inferred from GW observations of BNSs, especially when also measuring the NS EoS parameters. We pursue this objective using two sets of BNS events: one with 5 events and

the other with 50 events (including those 5 events), as detected during the O5 era by the LIGO and the Virgo detectors. The choice of 50 events, which is relatively high compared to the current merger rate, allows us to assess the statistical robustness of our methodology and investigate any potential systematic effects. However, we also study a more realistic number of detected BNS events for 5 to investigate the expected recovery of population, cosmology, and NS EoS. The choice of 5 detected BNS events with the network $\text{SNR} \geq 20$, following the Gaussian and double Gaussian mass distributions, corresponds to the merger rates of $R_0 \sim 1200 \text{ Gpc}^{-3} \text{yr}^{-1}$ and $R_0 \sim 700 \text{ Gpc}^{-3} \text{yr}^{-1}$ respectively, assuming the O5 run is planned for 2 years [55]. We consider 2 different mass models to examine the impact of mass distribution on inferring the cosmological and the NS EoS parameters. However, we do not explore the impact of different redshift evolution models in constraining hyperparameters since all our GW events are confined to the local Universe, i.e., within $\sim 350 \text{ Mpc}$.

A. Inference of Population & Cosmological Parameters

The methodology described in Sec. II is applied to a mock GW catalog of 5 and 50 BNS mergers detected during the O5 era. Initially, we study the influence of the NS EoS on inferring the population and the cosmological

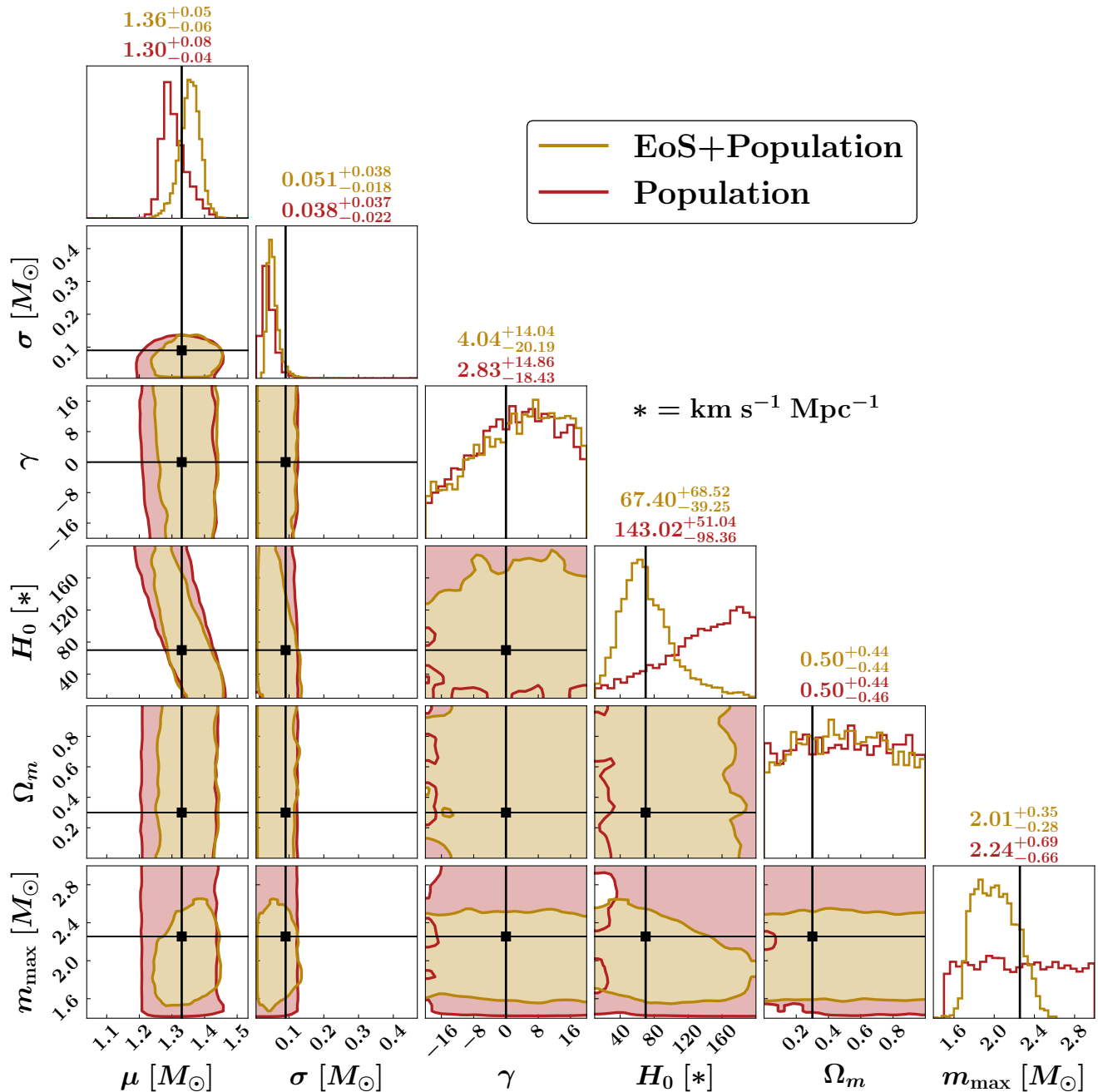


FIG. 1. Comparison of the inferred population and cosmological parameters from 5 events, based on the Gaussian mass distribution, detected by the LIGO-Virgo detectors. The black solid lines indicate the injected values of the corresponding parameters. The 90% credible intervals are shown for each of the respective marginalized one-dimensional posteriors.

parameters for BNSs, considering two different mass distributions: Gaussian and double Gaussian distributions. The Bayesian analysis is carried out both without and with accounting for the NS EoS. The former considers only mass and redshift information (m_1, m_2, z), while the latter also includes tidal parameters ($m_1, m_2, z, \Lambda_1, \Lambda_2$). In different figures of this paper, these analyses are referred to as ‘Population’ and ‘EoS+Population,’ respectively. Fig. 1 and Fig. 2 present the estimation of the

population and the cosmological parameters for 5 and 50 events, respectively, with BNSs following the Gaussian mass distribution. In both the figures, the population and the cosmological parameters are inferred using both approaches: ‘Population’ (considering only mass and redshift information) and ‘EoS+Population’ (including tidal parameters). Similar comparisons for BNSs with the double Gaussian mass distribution are shown in Fig. 3 and Fig. 4. The uncertainties corresponding to the 90% cred-

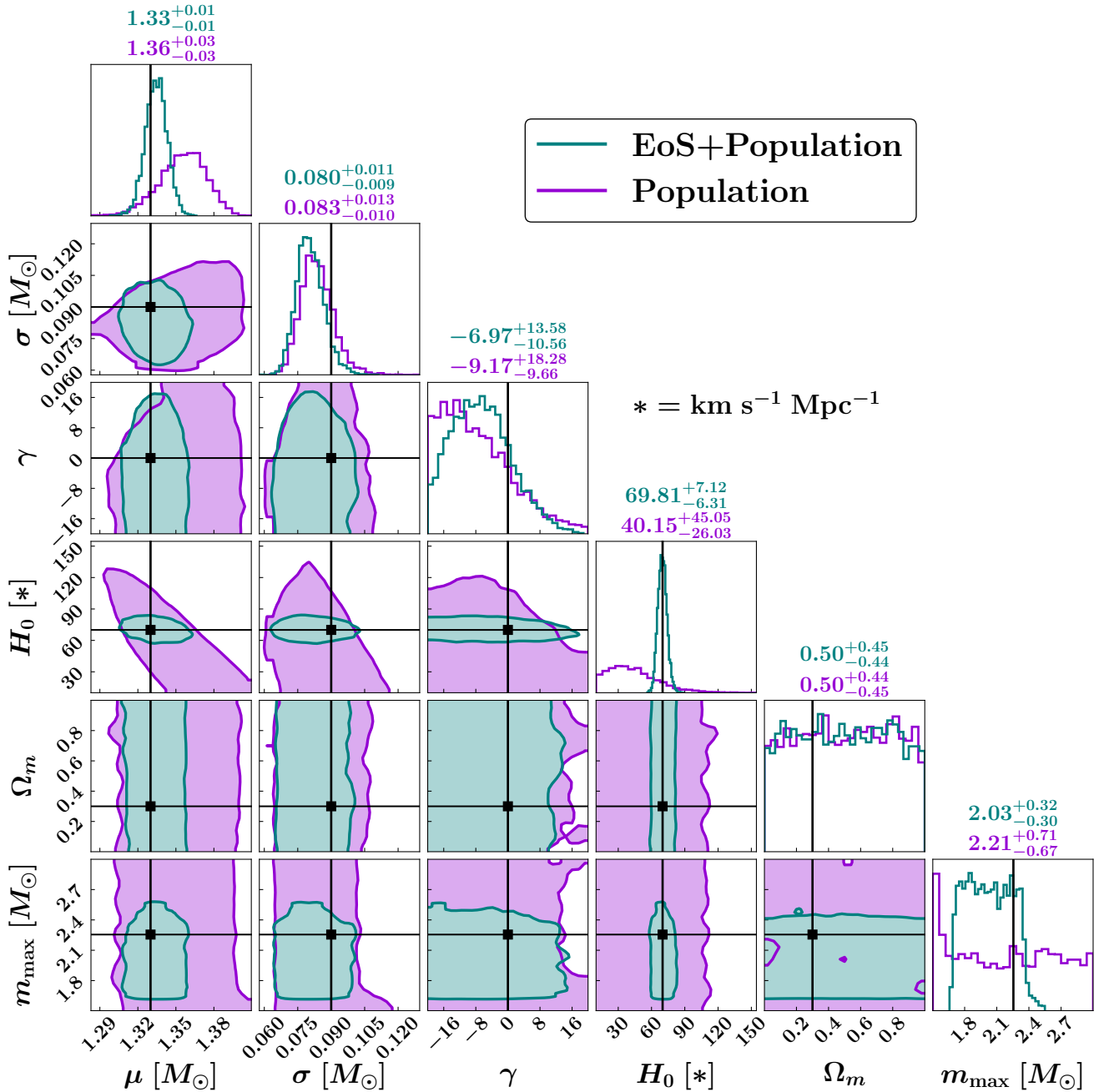


FIG. 2. Same as Fig. 1, but using 50 events.

ible intervals of all the population and the cosmological parameters are summarized in Table III.

Incorporating the NS EoS into the spectral siren method significantly improves the constraint on the Hubble constant. Notably, H_0 can not be constrained from 5 GW events, regardless of the mass distribution, when the NS EoS is not utilized. However, 50 events following both the mass distributions can infer H_0 without considering the NS EoS. Nevertheless, the precision of the H_0 measurement is significantly improved when the NS EoS is utilized, as shown in Fig. 2 and Fig. 4, corresponding

to the Gaussian and double Gaussian mass distributions, respectively.

The maximum mass, m_{\max} , is also expected to be well constrained when considering the NS EoS. The measurement of m_{\max} is related to the constraint of the NS EoS, which is discussed in Sec. V B. However, we briefly mention it here because it is relevant to the discussion of population and cosmology in this section. With a few GW events (5 events) alone, the maximum mass cannot be accurately inferred, as there are hardly any BNS near the maximum mass region for both mass distribu-

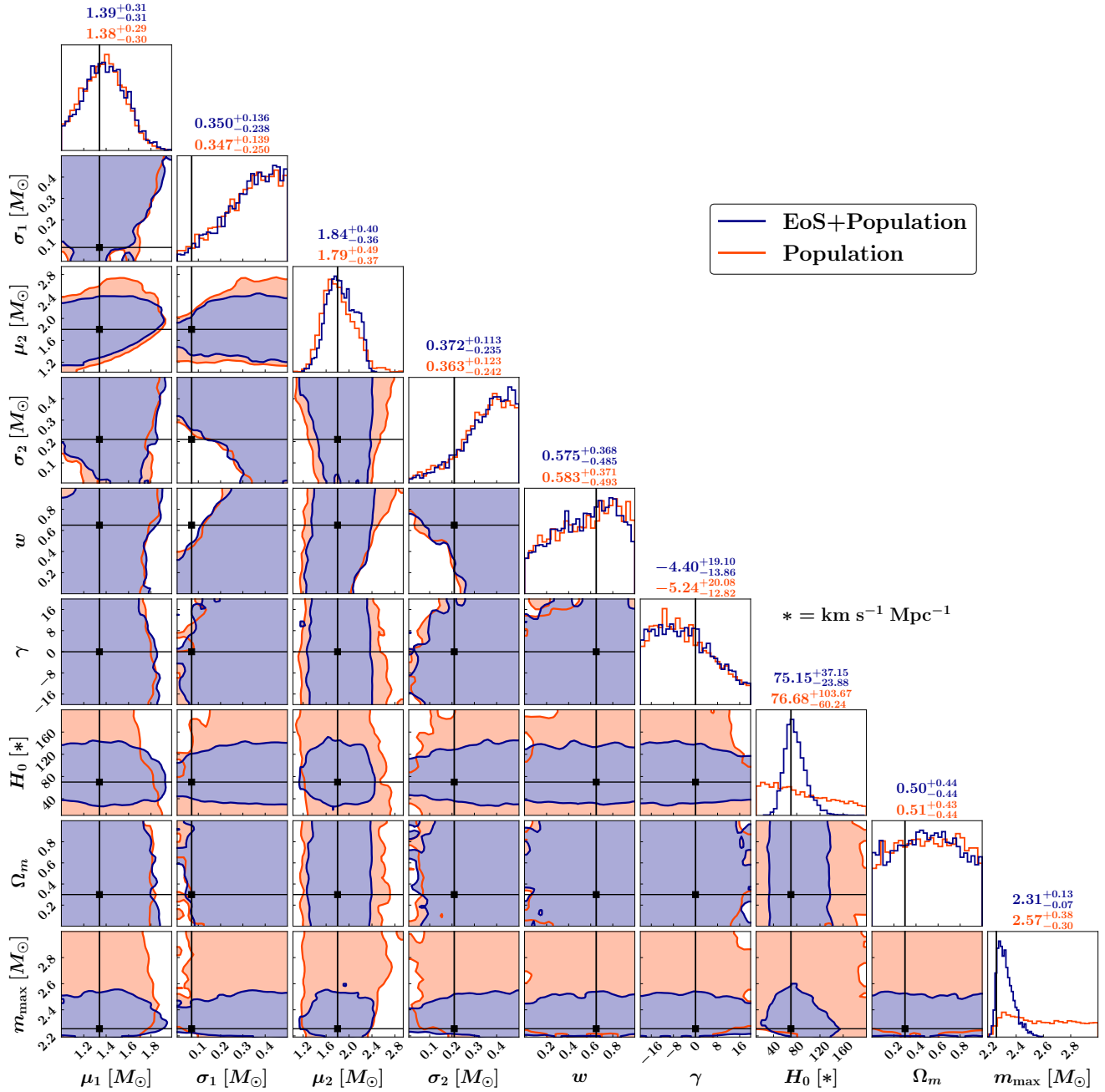


FIG. 3. Comparison of the inferred population and cosmological parameters from 5 GW events, following the double Gaussian mass distribution, detected by the LIGO-Virgo detectors. The black solid lines show the injected values of the corresponding parameters. The 90% credible intervals are also mentioned for each of the respective marginalized one-dimensional posteriors.

tions. Even with a larger set of GW events, m_{\max} remains weakly constrained due to the scarcity or absence of BNS mergers near m_{\max} . For instance, in the population of 50 BNS events with the Gaussian mass distribution, none of the NS source-frame masses exceeds $1.51 M_\odot$, as evident from the left panel of Fig. 12. Despite this limitation, m_{\max} is significantly constrained due to the incorporation of the NS EoS into the spectral siren method. In contrast, the spectral siren method alone cannot infer

m_{\max} in such cases. For the population of 50 BNSs characterized by the double Gaussian mass distribution, there are a few NSs near the maximum mass region (see the right panel of Fig. 12). The presence of relatively massive NSs further aids in constraining m_{\max} along with the constraints from the inferred NS EoS. Thus, the estimation of m_{\max} from the BNS population with the double Gaussian mass distribution is slightly more precise compared to that from the Gaussian mass distribution.

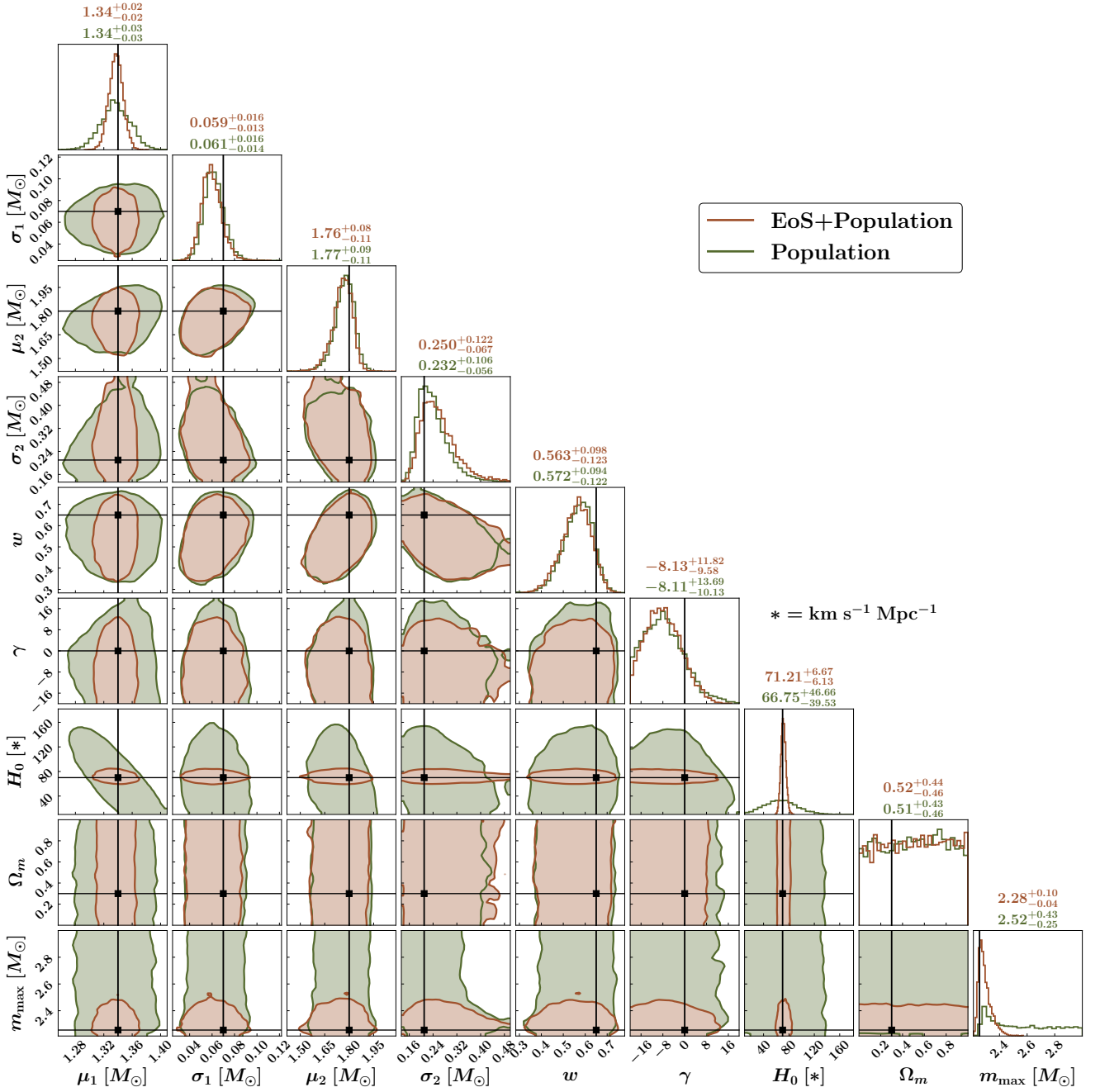


FIG. 4. Same as Fig. 3, but using 50 events.

Consequently, the measurement of the Hubble constant inferred from BNSs with the double Gaussian mass distribution marginally benefits from the improved constraint on m_{\max} .

Therefore, integrating the NS EoS into the Bayesian formalism can make a substantial impact on inferring the population and the cosmological parameters. Specifically, H_0 and m_{\max} are significantly constrained when considering the NS EoS, as summarized in Fig. 5. For a given NS EoS, the NS of (source-frame) mass m uniquely determines its tidal deformability Λ . This $m - \Lambda$ rela-

tion is determined by solving the Tolman-Oppenheimer-Volkoff (TOV) equations [63, 64] for a specific NS EoS, as elaborated in Appendix D.⁴ The observed component masses of the BNS events (which are redshifted) need to be converted to the source-frame masses using the corresponding distance posteriors from the GW obser-

⁴ In case no such $m - \Lambda$ correlations were accounted for, the posteriors of the source parameters from GW data would turn out to be as shown in Fig. 13 of Appendix C.

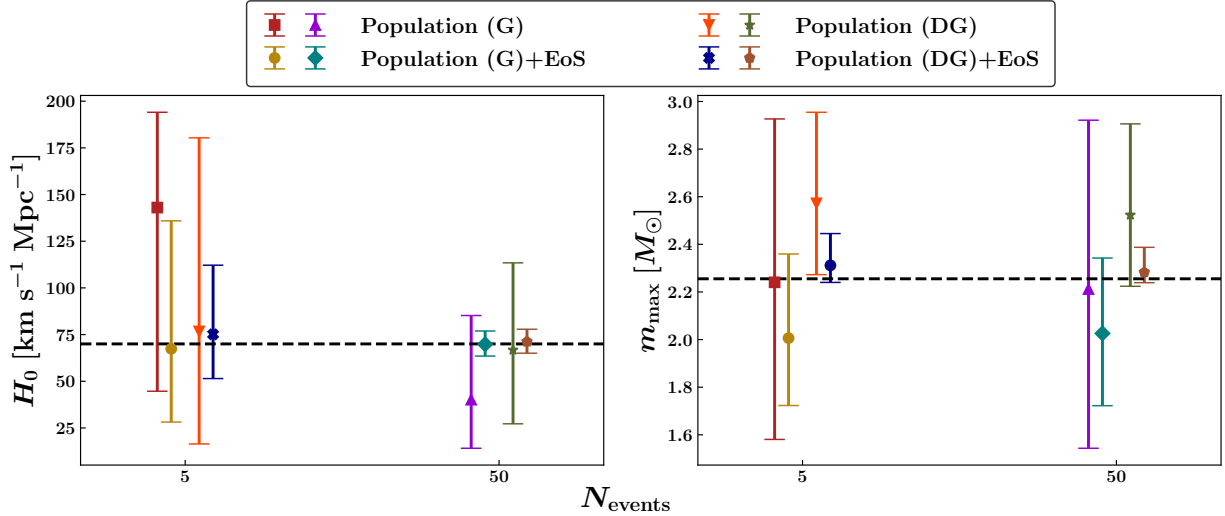


FIG. 5. Comparison of the uncertainty in measuring H_0 and m_{max} from 5 and 50 GW events, following the Gaussian (G) and double Gaussian (DG) mass distributions. The x-axis is not to scale.

Mass Model	Parameters	5 Events		50 Events	
		Population	EoS+Population	Population	EoS+Population
Gaussian	μ	$1.30^{+0.08}_{-0.04}$	$1.36^{+0.05}_{-0.06}$	$1.36^{+0.03}_{-0.03}$	$1.33^{+0.01}_{-0.01}$
	σ	$0.04^{+0.04}_{-0.02}$	$0.05^{+0.04}_{-0.02}$	$0.08^{+0.01}_{-0.01}$	$0.08^{+0.01}_{-0.01}$
	γ	$2.83^{+14.86}_{-18.43}$	$4.04^{+14.04}_{-20.19}$	$-9.17^{+18.28}_{-9.66}$	$-6.97^{+13.58}_{-10.56}$
	H_0	$143.02^{+51.04}_{-98.36}$	$67.40^{+68.52}_{-39.25}$	$40.15^{+45.05}_{-26.03}$	$69.81^{+7.12}_{-6.31}$
	Ω_m	$0.50^{+0.44}_{-0.46}$	$0.50^{+0.44}_{-0.44}$	$0.50^{+0.44}_{-0.45}$	$0.50^{+0.45}_{-0.44}$
	m_{max}	$2.24^{+0.69}_{-0.66}$	$2.01^{+0.35}_{-0.28}$	$2.21^{+0.71}_{-0.67}$	$2.03^{+0.32}_{-0.30}$
	Double Gaussian	μ_1	$1.38^{+0.29}_{-0.30}$	$1.39^{+0.31}_{-0.31}$	$1.34^{+0.03}_{-0.03}$
σ_1		$0.35^{+0.14}_{-0.25}$	$0.35^{+0.14}_{-0.24}$	$0.06^{+0.02}_{-0.01}$	$0.06^{+0.02}_{-0.01}$
μ_2		$1.79^{+0.49}_{-0.37}$	$1.84^{+0.40}_{-0.36}$	$1.77^{+0.09}_{-0.11}$	$1.76^{+0.08}_{-0.11}$
σ_2		$0.36^{+0.12}_{-0.24}$	$0.37^{+0.11}_{-0.24}$	$0.23^{+0.09}_{-0.06}$	$0.25^{+0.12}_{-0.07}$
w		$0.58^{+0.37}_{-0.49}$	$0.57^{+0.37}_{-0.48}$	$0.57^{+0.09}_{-0.12}$	$0.56^{+0.10}_{-0.12}$
γ		$-5.24^{+20.08}_{-12.82}$	$-4.40^{+19.10}_{-13.86}$	$-8.11^{+13.69}_{-10.13}$	$-8.13^{+11.82}_{-9.58}$
H_0		$76.68^{+103.67}_{-60.24}$	$75.15^{+37.15}_{-23.88}$	$66.75^{+46.66}_{-39.53}$	$71.21^{+6.67}_{-6.13}$
Ω_m		$0.51^{+0.43}_{-0.44}$	$0.50^{+0.44}_{-0.44}$	$0.51^{+0.43}_{-0.46}$	$0.52^{+0.44}_{-0.46}$
m_{max}		$2.57^{+0.38}_{-0.30}$	$2.31^{+0.13}_{-0.07}$	$2.52^{+0.43}_{-0.25}$	$2.28^{+0.10}_{-0.04}$

TABLE III. Comparison of the 90% credible interval corresponding to the uncertainty in measuring the population parameters with and without EoS parameters from GW events of 5 and 50, following Gaussian and double Gaussian mass distributions.

vations, necessitating knowledge of the Hubble constant. Thus, the Hubble constant is directly involved in deducing $m - \Lambda$ posteriors when a separate redshift measurement is not available. Conversely, NS EoS constraints help in the measurement of H_0 via $m - \Lambda$. Additionally, the NS EoS helps to constrain the maximum mass from GW observations since m_{max} is a derived parameter from the NS EoS rather than a free parameter. Including the NS EoS in the spectral siren method ensures that it is implemented in a way that remains consistent with the $m - \Lambda$ correlation that NSs are expected to obey. An EoS-informed application of the spectral siren method would, therefore, enhance the precision and accuracy of the inferred model parameters. The effectiveness of these improvements also varies with the mass distributions of

BNSs, as outlined previously.

However, the inference of the other cosmological parameter, Ω_m , does not improve even when incorporating the NS EoS. The calculation of luminosity distance is sensitive to Ω_m at high redshifts. However, all the GW events involved in this work are distributed in the low-redshift universe. Therefore, the impact of Ω_m on calculating the luminosity distance is negligible for the BNSs detected by the current-generation GW detectors, given their limited horizon distances. As a result, we cannot expect to infer Ω_m from these detections.

Similar to the improved estimation of H_0 and m_{max} , other mass model parameters are also expected to show improvements when considering the tidal information from GW observations due to the additional constraint

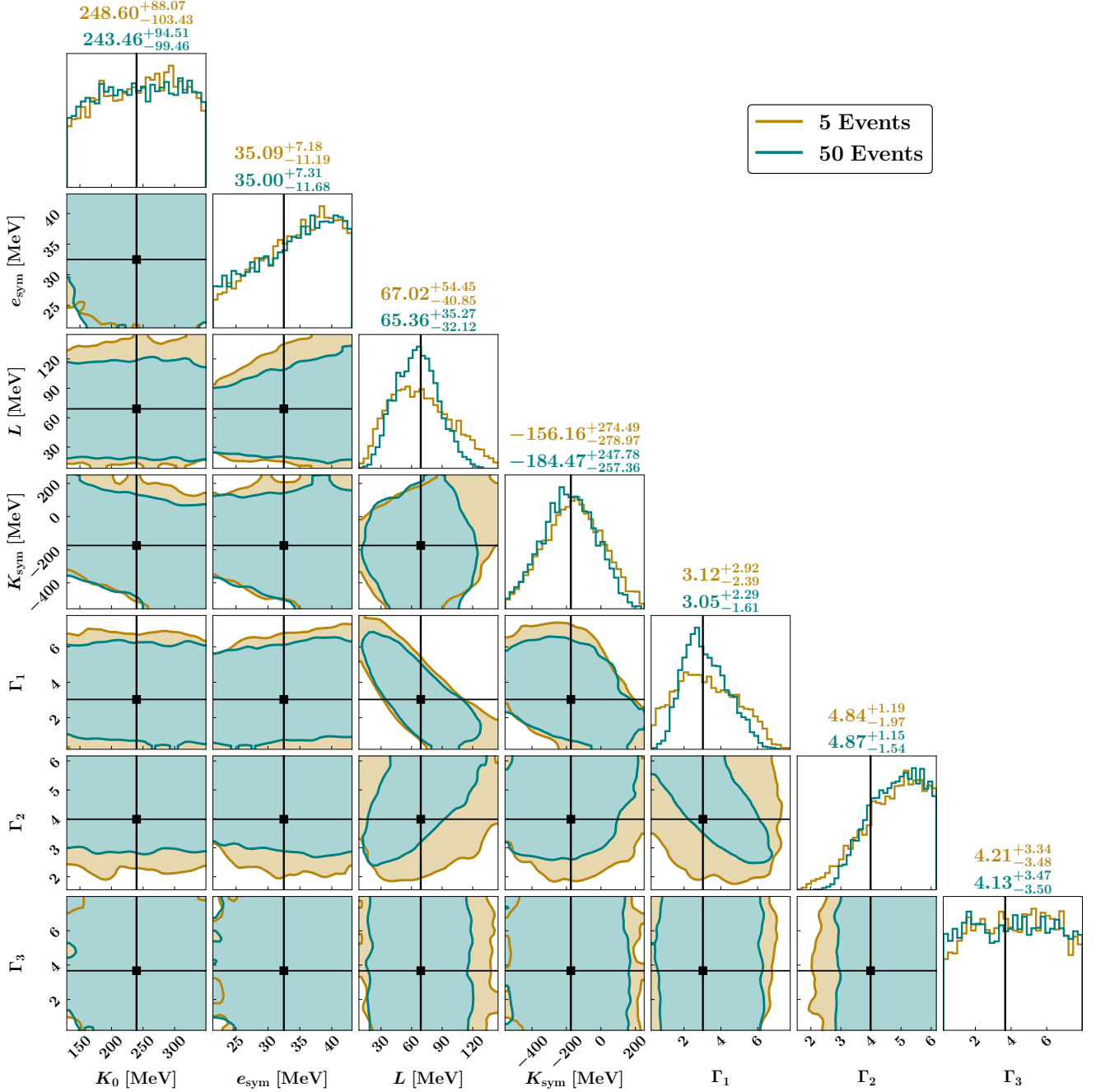


FIG. 6. Comparison of the constraints on the NS EoS parameters between 5 and 50 GW events, following the Gaussian mass distribution. The black solid lines correspond to the true NS EoS parameters. The uncertainty of each parameter, corresponding to the 90% credible interval is shown at the top of the respective marginalized 1D posterior.

from $m - \Lambda$ relations. The mean of the Gaussian (mass) distribution is inferred more precisely and accurately for 50 GW events when the NS EoS is considered (see Fig. 2). However, for 5 GW events with the same mass distribution, there is no significant impact on the estimation of μ . This is because the sample size of 5 GW events is too small to reflect the significance of μ inference from $m - \Lambda$ constraints. Moreover, a strong correlation be-

tween μ and H_0 is evident for both 5 and 50 events. As H_0 increases, the inferred redshift from the measured luminosity distance of the GW event also increases, leading to a decrease in the source-frame masses estimated from the observation of detector-frame masses. This implies a negative correlation between μ and H_0 . The correlations between μ and H_0 for 5 and 50 GW events are $r_{\mu, H_0}^{5\text{GW}} = -0.89$ and $r_{\mu, H_0}^{50\text{GW}} = -0.87$, respectively, when

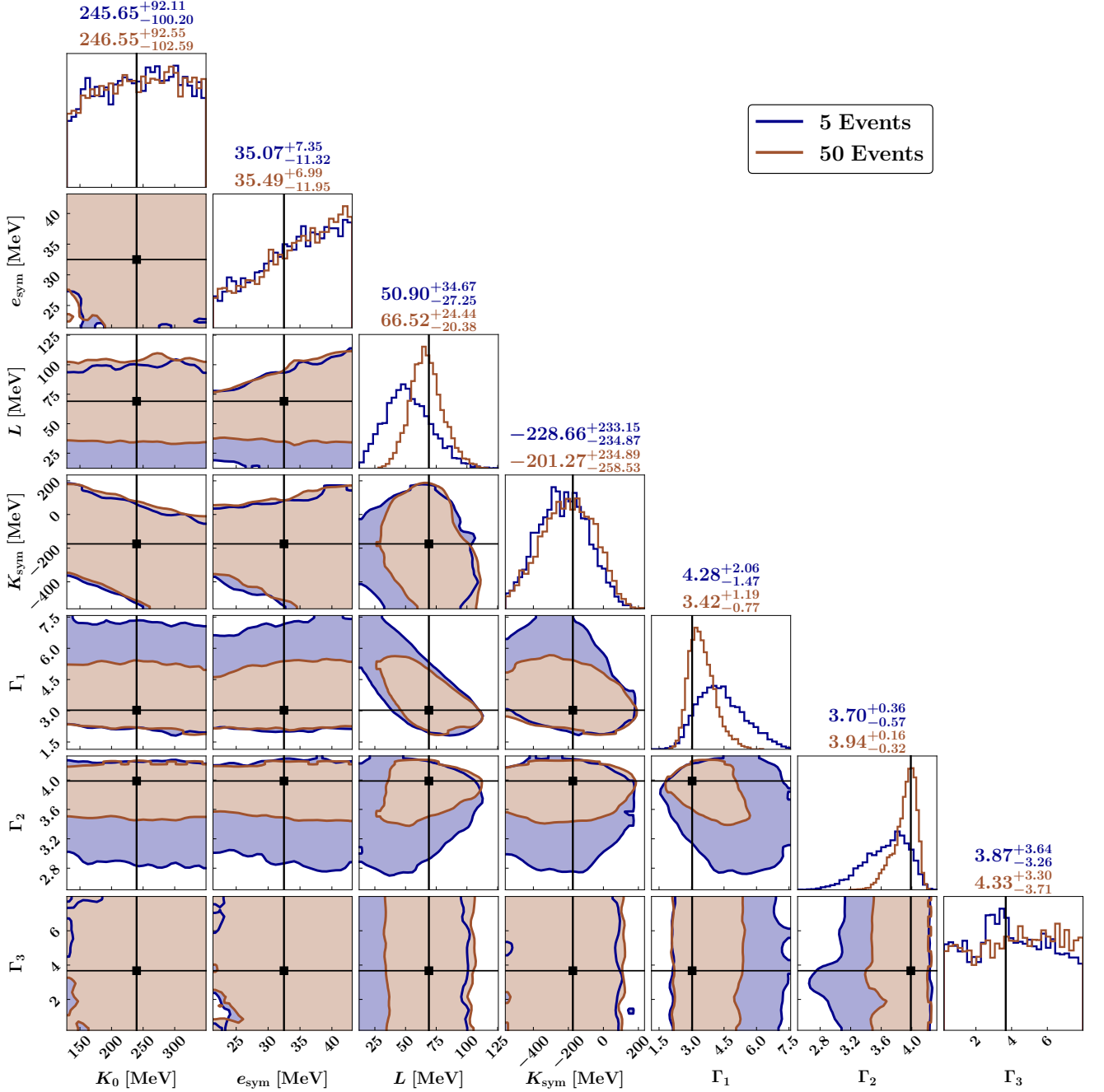


FIG. 7. Same as Fig. 6, but BNSs follow the double Gaussian mass distribution.

only the population is considered. A similar correlation between μ and H_0 is also reported in Ref. [27]. Due to the incorporation of additional information through tidal parameters of BNSs, the recovery of μ and H_0 is significantly improved, reducing the correlation between μ and H_0 to $\tilde{r}_{\mu, H_0}^{5\text{GW}} = -0.82$ and $\tilde{r}_{\mu, H_0}^{50\text{GW}} = -0.29$ for 5 and 50 events, respectively. This highlights the substantial impact of the NS EoS in diminishing the degree of correlation between μ and H_0 . Notably, the magnitude of the correlation for 5 GW events considering tidal

parameters is even less than that for 50 GW events without tidal parameters, i.e., $|\tilde{r}_{\mu, H_0}^{5\text{GW}}| < |\tilde{r}_{\mu, H_0}^{50\text{GW}}|$. The other mass distribution parameter σ , the standard deviation of the Gaussian distribution, remains similar, irrespective of the incorporation of the NS EoS. Though it is not constrained accurately for 5 GW events, its accuracy improves with the increase in the total number of GW events. However, the NS EoS has a marginal impact on the estimation of σ , as shown in the 1D marginalized posterior of σ in Fig. 2. It is expected that a larger number

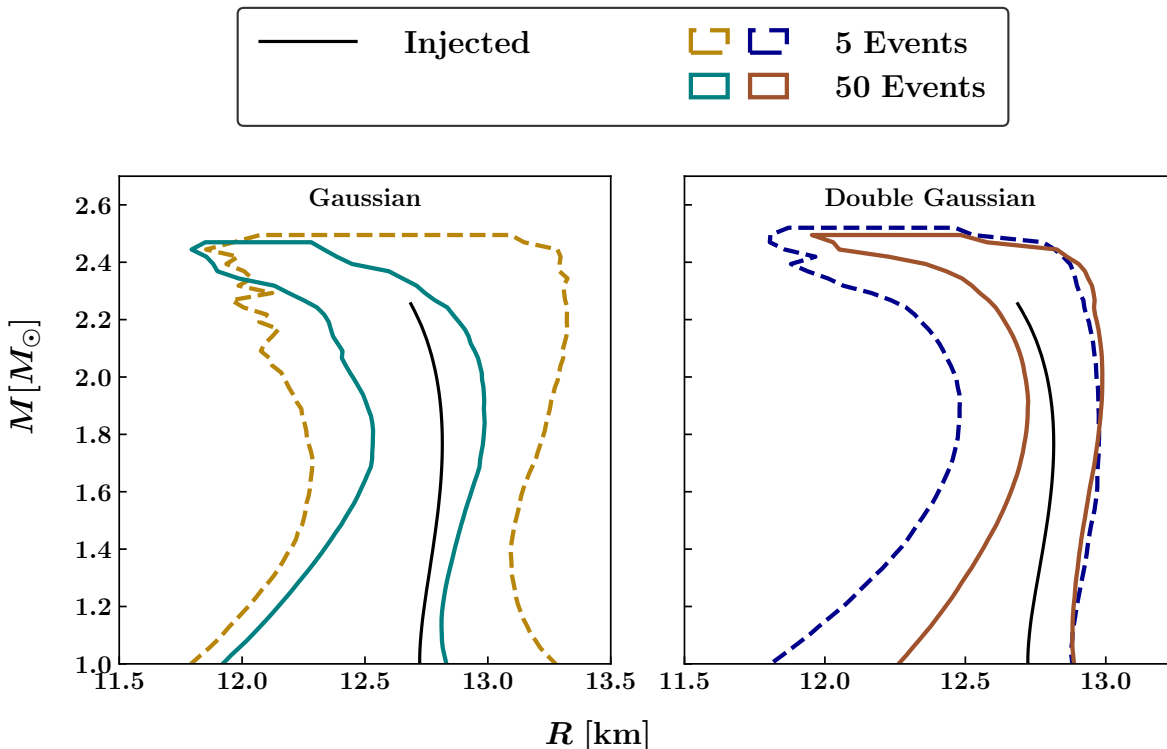


FIG. 8. 90% credible region of mass-radius posteriors, inferred from 5 and 50 GW events, following the Gaussian (left) and double Gaussian (right) mass distributions. The black solid line indicates the true mass-radius relation corresponding to the injected NS EoS parameters.

of BNS events would manifest the impact of the NS EoS in inferring σ significantly, which is currently beyond the scope of this work.

For the double Gaussian mass distribution, the posterior distributions of the parameters (μ_1, σ_1) for the first Gaussian component and (μ_2, σ_2) for the second Gaussian component are expected to exhibit similar characteristics to the posteriors of (μ, σ) , observed for the unimodal Gaussian mass distribution. This expectation stems from the nature of the double Gaussian distribution, which is a combination of two distinct Gaussian distributions. While the posterior of the first peak μ_1 of the double Gaussian mass distribution shows no impact from the consideration of the NS EoS (Fig. 3) for 5 GW events, μ_1 is constrained with better precision for 50 GW events when the NS EoS is taken into account. Similar to the correlation between μ and H_0 for BNS events with the Gaussian mass distribution, there exists a correlation between μ_1 and H_0 for BNS events following the double Gaussian mass distribution for the same reason. For the smaller number of GW events, i.e., 5, there is no strong correlation between μ_1 and H_0 ; the values of the correlation are $\tilde{r}_{\mu_1, H_0}^{5\text{GW}} = -0.07$ and $r_{\mu_1, H_0}^{5\text{GW}} = -0.24$, with and without considering the NS EoS, respectively. However, a relatively strong correlation $r_{\mu_1, H_0}^{50\text{GW}} = -0.87$ is evident for 50 GW events when only the population is considered. The degree of correlation is reduced when

the NS EoS is considered, as shown in the 2D joint posteriors of μ_1 and H_0 , with the corresponding value is $\tilde{r}_{\mu_1, H_0}^{50\text{GW}} = -0.18$. However, due to the presence of fewer GW events near the secondary peak ($\mu_2 = 1.8 M_\odot$) of the same mass distribution, even for the population of 50 events, there is no significant improvement in the inference of μ_2 or its correlation with H_0 . More events are required to have a significant number of BNSs at the secondary peak to observe a similar qualitative feature as seen for μ_1 . The other mass parameters, such as σ_1 , σ_2 , and w , do not benefit from the inclusion of the NS EoS parameters. Increasing the number of events allows for more precise constraints of these parameters due to reduced statistical uncertainty. However, σ_1 , σ_2 , and w remain poorly constrained with fewer events. To further explore the impact of the NS EoS in the inference of these parameters and understand the required number of events, a large number of simulated BNS events needs to be analyzed. Furthermore, the next-generation detectors can be considered in this context. We leave this exercise for future investigations.

The estimation of the redshift evolution parameter is difficult to constrain, irrespective of the choice of the mass distributions and the number of GW events. The redshift evolution parameter γ is weakly constrained because the redshift distribution of BNS is primarily limited to smaller luminosity distance ~ 350 Mpc. However, the

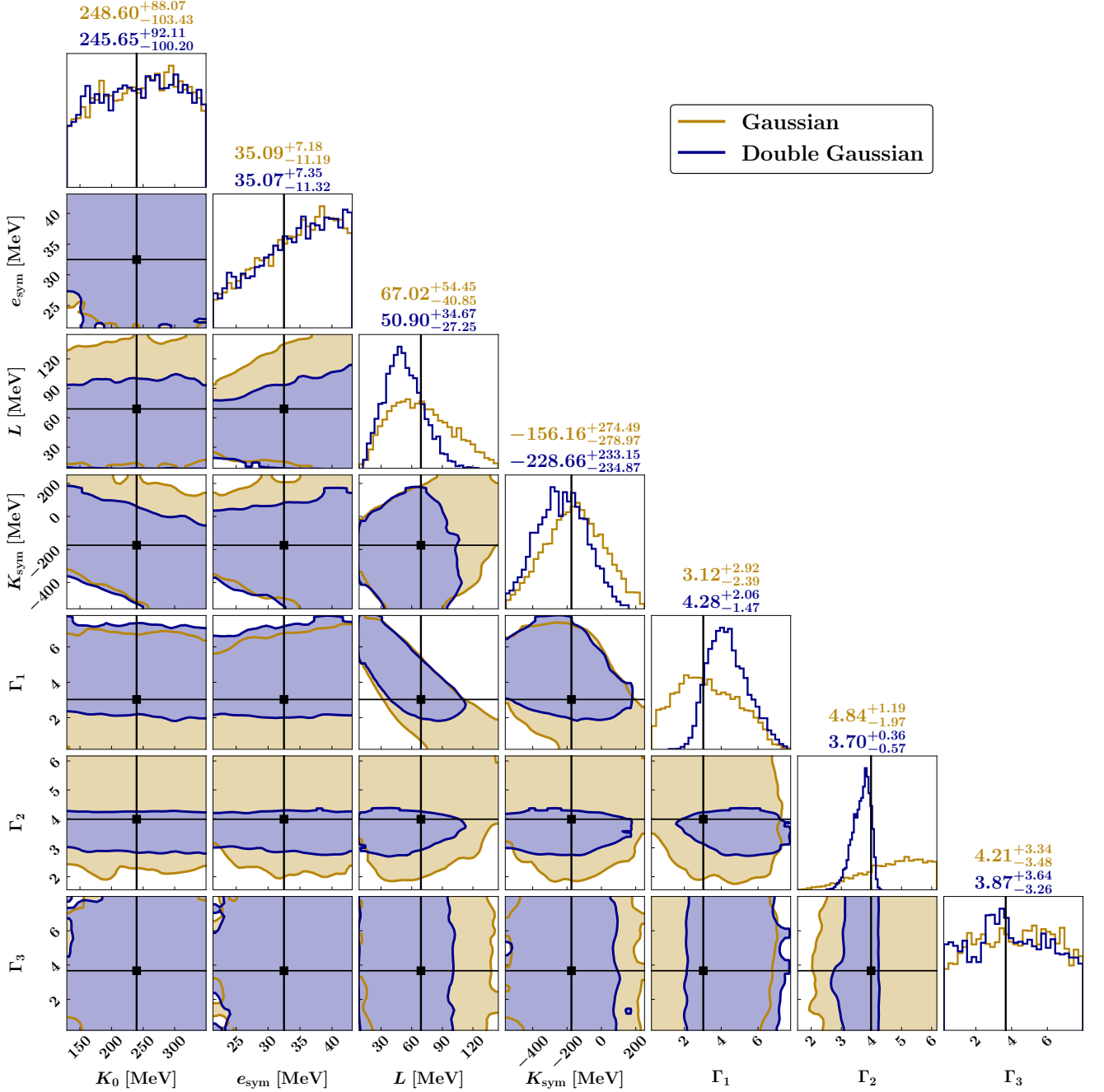


FIG. 9. Comparison of the constraints on the NS EoS parameters from 5 GW events, following the Gaussian and double Gaussian mass distributions. The black solid lines correspond to the true NS EoS parameters. The uncertainty of each parameter corresponding to the 90% credible interval is shown at the top of the 1D posterior for both mass distributions.

redshift distribution parameter shows an improvement in the precision when the number of detected GW events is increased from 5 to 50. Additionally, there is a slight enhancement in inferring γ for 50 GW events following the Gaussian mass distribution when the NS EoS is considered (see Fig. 2). Otherwise, we do not observe any significant impact of the NS EoS on inferring the redshift evolution parameter.

We find that the NS EoS strongly influences the precision and accuracy of the inferred population and cosmological parameters, particularly the Hubble constant and the maximum NS mass. However, its impact on the other population parameters describing mass and redshift distributions may vary depending on the chosen population model. These improvements stem from imposing $m - \Lambda$ relations derived from NS EoS into GW observations,

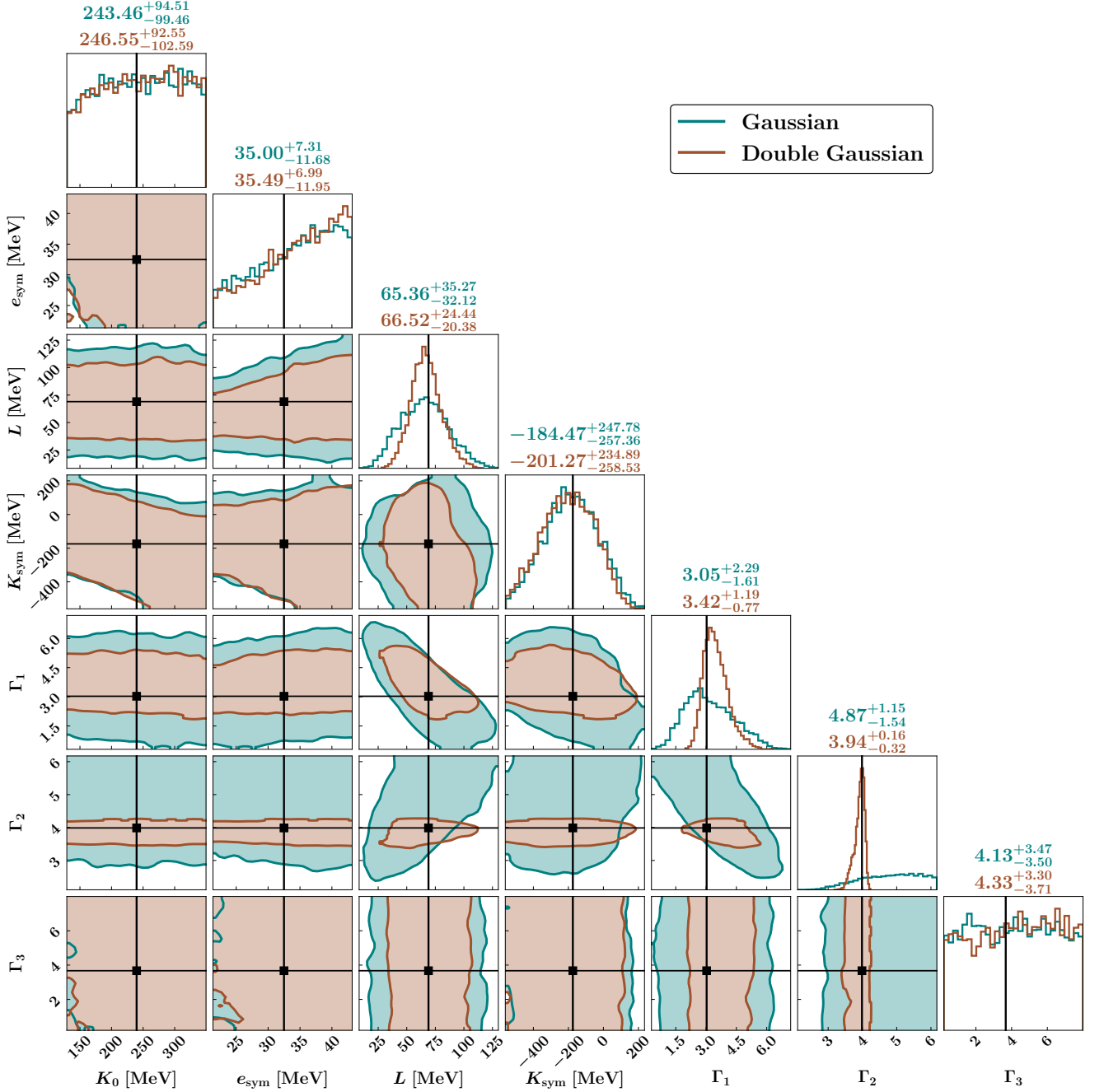


FIG. 10. Same as Fig. 9, but using 50 events.

which are not considered during the estimation of source parameters from GW data. Therefore, this study advocates for performing simultaneous inference of population, cosmology, and NS EoS for comprehensive analysis.

B. Constraint of NS EoS Parameters

The inferred NS EoS parameters from 5 and 50 events, following the Gaussian and double Gaussian mass distri-

butions, are shown in Fig. 6 and Fig. 7, respectively. It should be emphasized that we infer the NS EoS parameters together with the population and the cosmological parameters. However, for illustrative purposes, we do not show the joint posteriors of all the parameters, as they may not be adequately presented in the paper. Moreover, we do not find any significant correlations between the NS EoS parameters and the population or the cosmological parameters. Among the nuclear EoS parameters, K_0 and e_{sym} do not show any improvement with the increased

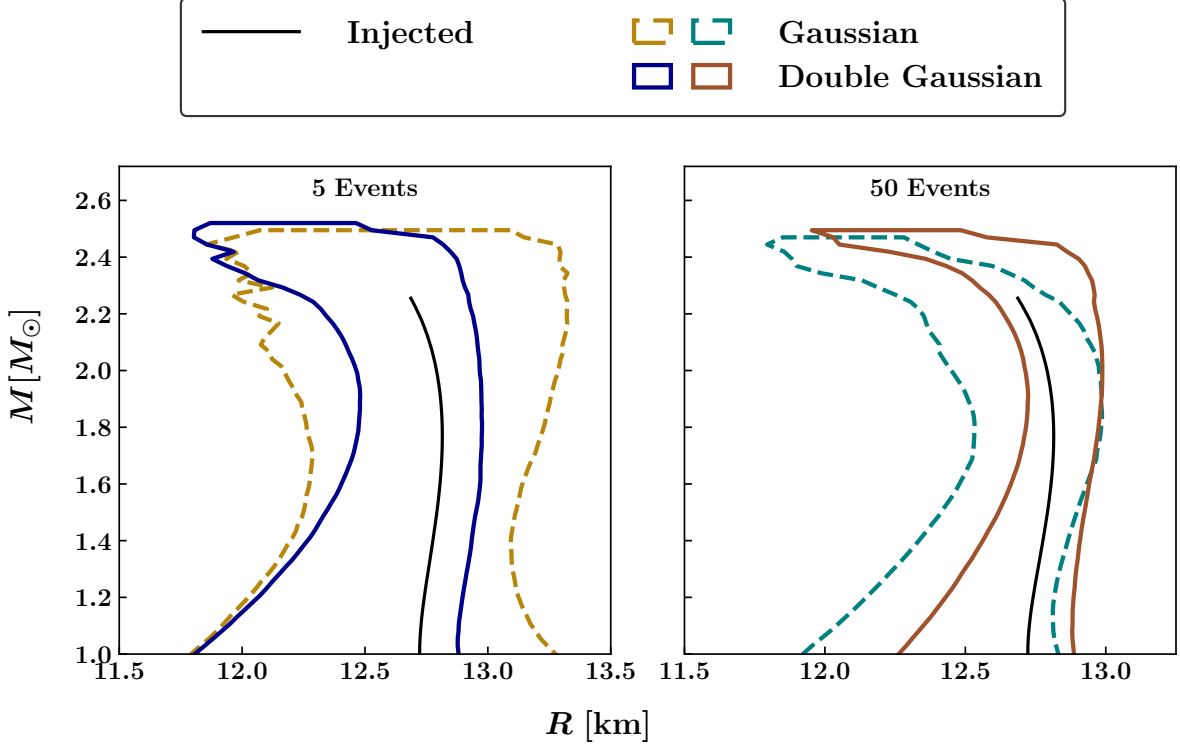


FIG. 11. Comparison of the 90% credible regions of mass-radius posteriors between the Gaussian and double Gaussian mass distributions, for 5 (left) and 50 (right) events. Unlike Fig. 8, which shows the credible regions separately for Gaussian and double Gaussian mass distributions, this figure provides a direct comparison between the two mass distributions for different numbers of GW events. The black solid line indicates the true mass-radius relation corresponding to the injected NS EoS parameters.

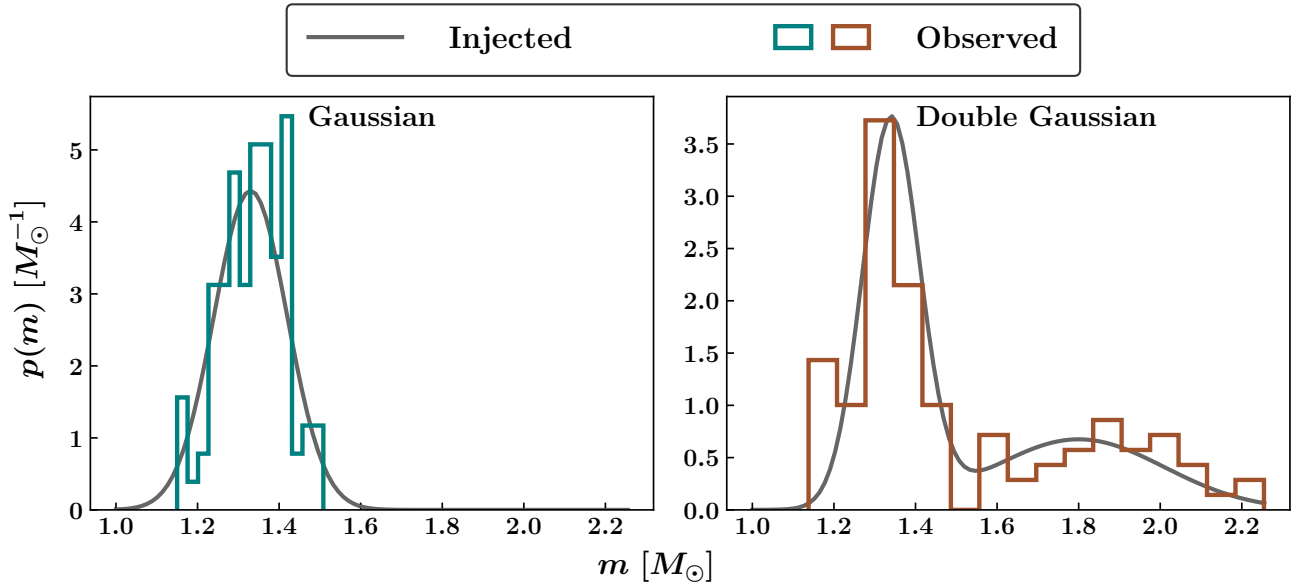


FIG. 12. Distribution of injected and observed component masses of NSs, following the Gaussian and double Gaussian mass distributions. The black solid lines represent the true mass distribution as specified by the parameters in Table II. The histograms show the distributions of source-frame masses for 50 NSs observed with $\text{SNR} \geq 20$.

EoS Parameters	Mass Model			
	Gaussian		Double Gaussian	
	5 Events	50 Events	5 Events	50 Events
K_0	$248.60^{+88.07}_{-103.43}$	$243.46^{+94.51}_{-99.46}$	$245.65^{+92.11}_{-100.20}$	$246.55^{+92.55}_{-102.59}$
e_{sym}	$35.09^{+7.18}_{-11.19}$	$35.00^{+7.31}_{-11.68}$	$35.07^{+7.35}_{-11.32}$	$35.49^{+6.99}_{-11.95}$
L	$67.02^{+54.45}_{-49.85}$	$65.36^{+35.27}_{-32.12}$	$50.90^{+34.67}_{-27.25}$	$66.52^{+24.44}_{-20.38}$
K_{sym}	$-156.16^{+274.49}_{-278.97}$	$-184.47^{+247.78}_{-257.36}$	$-228.66^{+233.15}_{-234.87}$	$-201.27^{+234.89}_{-258.53}$
Γ_1	$3.12^{+2.92}_{-2.39}$	$3.05^{+2.29}_{-1.61}$	$4.28^{+2.06}_{-1.47}$	$3.42^{+1.19}_{-0.77}$
Γ_2	$4.84^{+1.19}_{-1.97}$	$4.87^{+1.15}_{-1.54}$	$3.70^{+0.36}_{-0.57}$	$3.94^{+0.16}_{-0.32}$
Γ_3	$4.21^{+3.34}_{-3.48}$	$4.13^{+3.47}_{-3.50}$	$3.87^{+3.64}_{-3.26}$	$4.33^{+3.30}_{-3.71}$

TABLE IV. 90% credible intervals representing the uncertainty in measuring the EoS parameters from GW events of 5 and 50, following the Gaussian and double Gaussian mass distributions.

number of GW events, regardless of the mass distribution. The posteriors of these parameters are dominated by the effective priors of the EoS parameters, as shown in Fig. 14 of Appendix E. Consequently, the corresponding posteriors for 5 (50) events, following the Gaussian and double Gaussian mass distributions, are shown in Fig. 9 (Fig. 10). The posterior distributions of K_{sym} exhibit a slight improvement compared to the corresponding effective prior (see Fig. 14). The only nuclear parameter to be well constrained by these simulated GW observations is L . On the other hand, PP parameters Γ_1 and Γ_2 are well constrained, but Γ_3 is not constrained. This holds true irrespective of the number of GW events and the mass distribution of NSs. It has been demonstrated in Ref. [65] that most EoSs reach their maximum masses at densities lower than those where the last polytropic indices are attached. Hence, we cannot constrain Γ_3 . In other words, the hybrid nuclear+PP EoS parameterization can be modeled with fewer polytropic indices, thereby reducing computational time without significantly affecting the results. We present the 90% credible regions of the inferred mass-radius distributions in Fig. 8, which shows the impact of the number of GW events on constraining the mass-radius posteriors for both the mass distributions. From the mass-radius plots in Fig. 8, it is evident that the radius is not well constrained near the region of $\sim 1 M_\odot$. This is due to the fact that there are very few BNS events with at least one NS mass around $\sim 1 M_\odot$. The improvement in the mass-radius regions is expected to improve with a higher number of events due to the more precise inference of Γ_1 and Γ_2 .

We also investigate the impact of the mass distribution on inferring the NS EoS parameters, both for 5 and 50 GW events. The posteriors of the NS EoS parameters from 5 (50) events, following the Gaussian and double Gaussian mass distributions, are shown in Fig. 9 (Fig. 10). The comparison of mass-radius plots, as shown in Fig. 11, between the Gaussian and double Gaussian mass distributions for BNS events reveals that the mass-radius is not well constrained near the maximum mass for BNSs following the Gaussian mass distribution compared to the double Gaussian mass distribution. This result holds for both 5 and 50 events. BNS events fol-

lowing the double Gaussian mass distribution can relatively well constrain the mass-radius region, as shown in Fig. 11, irrespective of the number of events. This is expected because the NS EoS parameters Γ_1 and Γ_2 are constrained with better precision from the BNS events with the double Gaussian mass distribution compared to the Gaussian mass distribution. In particular, the presence of higher mass NSs in the double Gaussian mass distribution, compared to the Gaussian mass distribution (see, Fig. 12), contributes to better constraining some NS EoS parameters, and hence the mass-radius of NSs.

VI. CONCLUSION

In this work, we demonstrate the efficacy of simultaneous inference of population, cosmology, and NS EoS. This approach applies the spectral siren method exclusively to a population of binary neutron star signals by comparing the source-frame mass spectrum with the observed mass distribution. While doing so, it also utilizes the measured NS tidal parameters along with the $m - \Lambda$ constraints to estimate the population and cosmological parameters. Our study shows that the spectral siren method can constrain H_0 with 50 events distributed within ~ 350 Mpc. However, it fails to constrain it when the population is limited to just 5 BNSs, which is the expected number in the O5 era. Moreover, m_{max} remains poorly constrained due to the paucity or absence of BNS events near the maximum NS mass region of our simulations. Incorporating the NS EoS parameters into the spectral siren method explicitly imposes the $m - \Lambda$ constraints through the NS EoS by including the tidal parameters of BNSs with their observed masses and luminosity distances. This additional $m - \Lambda$ relation, in conjunction with cosmology (especially H_0), helps to break the mass-redshift degeneracy in the observed source parameters of GW data. Thus, including tidal parameters in the spectral siren method significantly improves the inference of H_0 , as well as a more precise estimation of m_{max} . Moreover, incorporating the NS EoS also benefits the measurability of certain population parameters. Therefore, this work recommends inferring cosmological parameters

alongside population and NS EoS parameters to improve the precision and accuracy of model parameters.

However, except for m_{\max} , improvements in the measurement of population parameters are not as significant as that of H_0 . This is due to significant uncertainties in the source parameters and the limited number of BNS mergers – as expected for the current-generation detectors. In future-generation detectors, where the precise measurements of source parameters for a large number of events will cause systematics to dominate over statistical uncertainties, this method will become more important. Neglecting the $m - \Lambda$ relations from the NS EoS in such cases will bias model parameters. Nonetheless, the method is essential for estimating the Hubble constant from BNS events observed as dark sirens by the current-generation detectors.

This study of simulated BNS events shows that most nuclear parameters in the EoS model are not constrained by the GW events observed with the current-generation detectors. However, one can employ informed priors over K_0 , e_{sym} , and L , derived from laboratory-based nuclear experiments, e.g., PREX [66]/CREX [67], and theoretical predictions performed by chiral effective field theory [68, 69], to improve the precision of estimating model parameters. This approach also updates the constraints on nuclear parameters obtained thus far from GW observations. Moreover, an informed prior by combining other observations related to the NS properties, such as mass-radius measurements [70–73] from X-ray observations and maximum mass thresholds from radio pulsar measurements [74], can aid in precisely measuring the Hubble constant. Thus, our method may enable accurate and precise determination of the Hubble constant by integrating data from nuclear experiments and various astrophysical observations, including X-ray and radio data, with GW data.

The method proposed in this study can be generalized to any parameterized model, encompassing population, cosmology, and NS EoS. We consider that both components of BNS follow the same mass distribution. However, there is also evidence from galactic BNS observations that they may come from separate mass distributions [47]. Additionally, we take our NSs to be non-spinning: It is important to consider realistic spin models since spin mis-modeling can also lead to biased estimation of mass distributions [75]. Our method can easily be extended to incorporate different parameterized population models in the Bayesian formalism. The precision and accuracy of inferring different hyperparameters may vary depending on the choice of models. We have also made a simplified assumption regarding the redshift evolution model as a power law with $\gamma = 0$ as an injected parameter. Even for real observations with the current-generation detectors, the power law distribution is reasonable as all the BNSs are distributed within the low-redshift Universe. The choice of γ may impact the accuracy and precision of estimated model parameters. However, it is difficult to infer the redshift evolution pa-

parameter with significant precision and accuracy with a small number of BNS events, which is expected with current-generation detectors due to the smaller horizon redshift.

In this work, we consider the network of 3 detectors, consisting of two LIGO detectors and the Virgo detector. We can expect a more precise estimation of the Hubble constant with the addition of KAGRA [76] and LIGO-India [77] to the detector network, which is a possible scenario for future observations. Incorporating additional detectors can alleviate the degeneracy between luminosity distance and inclination angle [78], leading to a significant improvement in the measurement of the Hubble constant. Additionally, including more detectors helps with the more precise inference of the redshift evolution parameter(s), which is not achieved in this work. One can explore the prospect of improvements in different hyperparameters with various detector-network configurations, which is not currently part of this work.

Projecting further, in the next-generation ground-based detectors, such as the Cosmic Explorer [79] and the Einstein Telescope [80], which are planned for the next decade, a large number of BNSs $\sim 10^5$ is expected to be detected per year [81]. Since only a small fraction of the total events is expected to be bright standard sirens up to a relatively small redshift of $z \sim 2$ [82], compared to the horizon redshift of $z \sim 10$ for the next-generation detectors, most of the detected BNS mergers will remain dark sirens. This is due to the coverage limitation of the future spectroscopic galaxy surveys [83]. In such circumstances, the method discussed in this paper is particularly beneficial for probing cosmology as well as mass and redshift distributions. Since the horizon redshift is quite large, this method also enables the probing of different cosmological parameters such as the matter density and the dark energy equation of state, which are not possible with the current-generation detectors. One must be careful to account for the impact of lensing [84] of GW signals while performing our method for the next-generation detectors to ensure the unbiased estimation of NS EoS, population, and cosmology. However, this concern is not important for the current-generation detectors due to their small horizon distance of $d_L \sim 350$ Mpc. However, it is not trivial to estimate population, NS EoS, and cosmology from the observations of dark BNS mergers, some of which may be lensed. The incorporation of EoS may mitigate the systematics due to lensing in inferring different model parameters, which can be explored in future studies.

ACKNOWLEDGMENTS

The authors would like to thank Simone Mastrogianni for assessing the manuscript as part of the LSC internal review. T.G. gratefully acknowledges the computational facilities provided by IUCAA, including the LDG cluster Sarathi and Pegasus, as well as the use of

the LDG cluster Hawk at Cardiff University, supported by STFC grants ST/I006285/1 and ST/V005618/1. B.B. acknowledges the support from the Knut and Alice Wallenberg Foundation under grant Dnr. KAW 2019.0112 and the Deutsche Forschungsgemeinschaft (DFG, German Research Foundation) under Germany's Excellence Strategy – EXC 2121 “Quantum Universe” – 390833306. S. B. acknowledges support from the NSF under Grant PHY-2309352. S.J.K gratefully acknowledges support from SERB Grants SRG/2023/000419 and MTR/2023/000086.

Appendix A: Bayesian Framework

In this appendix, we briefly review the Bayesian inference of model parameters $\mathbf{\Lambda}$ from GW data. According to Bayes' theorem, we can write the posterior probability distribution of $\mathbf{\Lambda}$ for a set of GW data $\{d\}$ as follows:

$$p(\mathbf{\Lambda} | \{d\}) = \frac{\mathcal{L}(\{d\} | \mathbf{\Lambda})p(\mathbf{\Lambda})}{Z(\{d\})}, \quad (\text{A1})$$

$$\mathcal{L}(d | \Lambda) = p(\mathbf{\Lambda}) \int dm_1 \int dm_2 \int dz \int d\Lambda_1 d\Lambda_2 \mathcal{L}(d | \boldsymbol{\theta}) p(m_1, m_2, \Lambda_1, \Lambda_2 | \mathbf{\Lambda}_m, \mathbf{\Lambda}_\mathcal{E}) p(z | \mathbf{\Lambda}_z), \quad (\text{A4})$$

where $p(\mathbf{\Lambda}) = p(\mathbf{\Lambda}_m)p(\mathbf{\Lambda}_z)p(\mathbf{\Lambda}_c)p(\mathbf{\Lambda}_\mathcal{E})$ denotes the prior over model hyperparameters $\mathbf{\Lambda}$. Given that the tidal de-

$$\mathcal{L}(d | \Lambda) = p(\mathbf{\Lambda}) \int dm_1 \int dm_2 \int dz \mathcal{L}(d | m_1, m_2, z, \Lambda_1(m_1, \mathbf{\Lambda}_\mathcal{E}), \Lambda_2(m_2, \mathbf{\Lambda}_\mathcal{E})) p(m_1, m_2 | \mathbf{\Lambda}_m) p(z | \mathbf{\Lambda}_z), \quad (\text{A5})$$

as,

$$p(m_1, m_2, \Lambda_1, \Lambda_2 | \mathbf{\Lambda}_m, \mathbf{\Lambda}_\mathcal{E}) = p(m_1, m_2 | \mathbf{\Lambda}_m) \times \delta(\Lambda_1 - \Lambda_1(m, \mathbf{\Lambda}_\mathcal{E})) \delta(\Lambda_2 - \Lambda_2(m, \mathbf{\Lambda}_\mathcal{E})). \quad (\text{A6})$$

It is important to note that we do not incorporate $\mathbf{\Lambda}_\mathcal{E}$ when we only focus on population and cosmology, as already mentioned in Sec. II. So, we exclude tidal parameters from the set of source parameters.

Appendix B: Detector-Frame to Source-Frame

In hierarchical inference, it is necessary to remove the effect of the prior to calculate the likelihood (see Eq. (2)). In this work, we have imposed uniform priors over detector-frame chirp mass (\mathcal{M}^z) and mass ratio

where $\mathcal{L}(\{d\} | \mathbf{\Lambda})$ denotes the joint likelihood, which is defined as the product of the individual event likelihood:

$$\mathcal{L}(\{d\} | \mathbf{\Lambda}) = \prod_i \mathcal{L}(d_i | \mathbf{\Lambda}). \quad (\text{A2})$$

Here, i indicates the i th GW event. For the rest of the calculation, we drop the use of i for notational convenience. The individual event likelihood $\mathcal{L}(d | \mathbf{\Lambda})$ is computed from measurements of the source parameters $\boldsymbol{\theta}$:

$$\mathcal{L}(d | \Lambda) = \int \mathcal{L}(d | \boldsymbol{\theta}) p(\boldsymbol{\theta} | \Lambda) d\boldsymbol{\theta} \quad (\text{A3})$$

Here, the second term $p(\boldsymbol{\theta} | \Lambda)$ represents the model prior. The above equation can be further simplified by considering different model parameters $\mathbf{\Lambda} = \{\mathbf{\Lambda}_\mathcal{E}, \mathbf{\Lambda}_m, \mathbf{\Lambda}_z, \mathbf{\Lambda}_c\}$ and source parameters $\boldsymbol{\theta} = \{m_1, m_2, z, \Lambda_1, \Lambda_2\}$ explicitly:

formability is mass-dependent for a specific equation of state $\mathbf{\Lambda}_\mathcal{E}$, Eq. (A4) can be further simplified when considering NS tidal parameters,

(q); cosmology independent d_L^2 prior over luminosity distance. However, our analysis is based on the source-frame parameters. For the given prior probability defined on (\mathcal{M}^z, q, d_L) , the corresponding probability in (m_1, m_2, z) is

$$p(m_1, m_2, z) = p(\mathcal{M}^z, q, d_L) \left| J \left(\frac{\mathcal{M}^z, q, d_L}{m_1, m_2, z} \right) \right| \propto d_L^2 (1+z) \frac{\partial d_L}{\partial z} \frac{(m_1 m_2)^{3/5}}{m_1^2 (m_1 + m_2)^{1/5}} \quad (\text{B1})$$

where $|J|$ denotes the determinant of the Jacobian matrix J . In Eq. (B1), the first term comes from the d_L^2 prior, and the rest of the expression can be obtained by simplifying the following Jacobian, corresponding to the coordinate transformation from (\mathcal{M}^z, q, d_L) to (m_1, m_2, z) :

$$J\left(\frac{\mathcal{M}^z, q, d_L}{m_1, m_2, z}\right) = \begin{bmatrix} \frac{\partial \mathcal{M}^z}{\partial m_1} & \frac{\partial \mathcal{M}^z}{\partial m_2} & \frac{\partial \mathcal{M}^z}{\partial z} \\ \frac{\partial q}{\partial m_1} & \frac{\partial q}{\partial m_2} & \frac{\partial q}{\partial z} \\ \frac{\partial d_L}{\partial m_1} & \frac{\partial d_L}{\partial m_2} & \frac{\partial d_L}{\partial z} \end{bmatrix} \quad (\text{B2})$$

Using the definitions of luminosity distance (Eq. (14)) and comoving distance ($d_c = d_L/(1+z)$), Eq. (B1) can be written as

$$p(m_1, m_2, z) \propto d_L^2(1+z) \left[d_c + \frac{c(1+z)}{H(z)} \right] \left[\frac{(m_1 m_2)^{3/5}}{m_1^2(m_1 + m_2)^{1/5}} \right] \quad (\text{B3})$$

Appendix C: Posteriors of Single GW Event

In this appendix, we show the posterior distributions of the source parameters of a BNS merger in Fig. 13. Though we perform sampling in the observed chirp mass and mass ratio to estimate the source-parameters for computational efficiency, we show the component masses (in the detector-frame) to illustrate that the posteriors of the source parameters exhibit no correlation between mass and tidal parameters, as determined by the NS EoS.

Appendix D: Calculation of Neutron Star Radius and Tidal Deformability

The structure of neutron stars is described by the Tolman-Oppenheimer-Volkoff (TOV) equations [63, 64], which are derived from the general relativistic equations for hydrostatic equilibrium. With $G = 1$ and $c = 1$, the TOV equations simplify to:

$$\frac{dp(r)}{dr} = -\frac{(\epsilon(r) + p(r))(m(r) + 4\pi r^3 p(r))}{r(r - 2m(r))} \quad (\text{D1})$$

$$\frac{dm(r)}{dr} = 4\pi r^2 \epsilon(r) \quad (\text{D2})$$

where $p(r)$ is the pressure, $\epsilon(r)$ is the energy density, and $m(r)$ is the mass enclosed within the radius r . These equations are solved with an appropriate equation of state (EoS) that relates the pressure to the energy density.

The radius R of the neutron star is determined by the point at which the pressure drops to zero, i.e., $p(R) = 0$.

The tidal deformability [85–87] Λ of a neutron star is a measure of its deformation in response to an external tidal field and is defined as:

$$\Lambda = \frac{2}{3} k_2 \left(\frac{R}{M} \right)^5 \quad (\text{D3})$$

where k_2 is the second Love number, R is the radius, and M is the mass of the neutron star. The second Love number k_2 is calculated using:

$$k_2 = \frac{8C^5}{5} (1 - 2C)^2 [2 + 2C(y_R - 1) - y_R] \times \{2C[6 - 3y_R + 3C(5y_R - 8)] + 4C^3[13 - 11y_R + C(3y_R - 2) + 2C^2(1 + y_R)] + 3(1 - 2C)^2[2 - y_R + 2C(y_R - 1)] \log(1 - 2C)\}^{-1} \quad (\text{D4})$$

where $C = \frac{M}{R}$ is the compactness parameter, and y_R is determined by solving the following differential equation simultaneously with the TOV equations:

$$\frac{dy(r)}{dr} = -\frac{y(r)^2}{r} - \frac{y(r)}{r} [1 + 4\pi r^2 (p(r) - \epsilon(r))] - \frac{4\pi r^2 \left(5\epsilon(r) + 9p(r) + \frac{\epsilon(r) + p(r)}{\partial p(r)/\partial \epsilon(r)} - \frac{6}{4\pi r^2} \right)}{r - 2m(r)} + \frac{4(m(r) + 4\pi r^3 p(r))}{r(r - 2m(r))} \quad (\text{D5})$$

with the boundary condition $y(0) = 2$. The value of y_R is obtained at the star's surface $r = R$.

By solving the TOV equations along with the above differential equation for $y(r)$, one can obtain the radius R and the Love number k_2 . Subsequently, these quantities can be used to calculate the tidal deformability Λ .

Appendix E: Effective Priors over NS EoS Parameters

We employ uniform priors for the EoS parameters, as detailed in Table II. However, not all parameter combinations are physically viable, as a crust-core junction density must be identified. As a result, some parameter combinations are redundant. Given that the fixed BPS crust is matched with the empirical parameterization, the effective priors for the EoS parameters, particularly the empirical parameters, are no longer uniformly distributed, as shown in Fig. 14.

[1] Adam G. Riess *et al.*, “A Comprehensive Measurement of the Local Value of the Hubble Constant with 1 km s⁻¹

Mpc⁻¹ Uncertainty from the Hubble Space Telescope and the SH0ES Team,” *Astrophys. J. Lett.* **934**, L7 (2022),

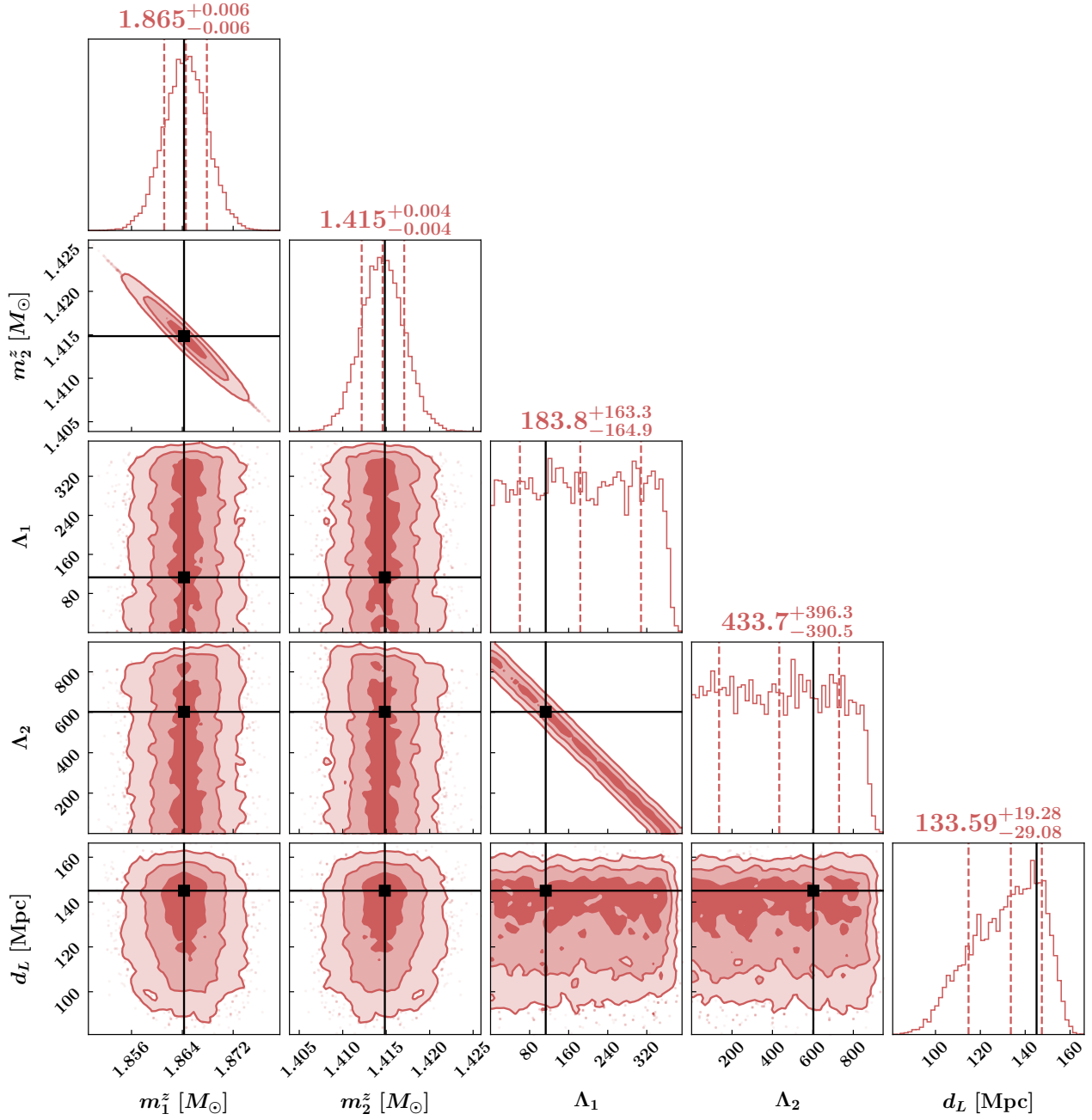


FIG. 13. Marginalized joint posteriors of redshifted component masses (m_1^z and m_2^z), their corresponding tidal deformabilities (Λ_1 and Λ_2), and luminosity distance (d_L) inferred from GW data of a BNS. The black vertical and horizontal solid lines represent the injected values of the corresponding parameters.

- arXiv:2112.04510 [astro-ph.CO].
- [2] N. Aghanim *et al.* (Planck), “Planck 2018 results. VI. Cosmological parameters,” *Astron. Astrophys.* **641**, A6 (2020), [Erratum: *Astron. Astrophys.* 652, C4 (2021)], arXiv:1807.06209 [astro-ph.CO].
- [3] J. Aasi *et al.* (LIGO Scientific), “Advanced LIGO,” *Class. Quant. Grav.* **32**, 074001 (2015), arXiv:1411.4547 [gr-qc].
- [4] F. Acernese *et al.* (VIRGO), “Advanced Virgo: a second-generation interferometric gravitational wave detector,” *Class. Quant. Grav.* **32**, 024001 (2015), arXiv:1408.3978 [gr-qc].
- [5] B. P. Abbott *et al.* (LIGO Scientific, Virgo), “GW170817: Observation of Gravitational Waves from a Binary Neutron Star Inspiral,” *Phys. Rev. Lett.* **119**, 161101 (2017), arXiv:1710.05832 [gr-qc].
- [6] B. P. Abbott *et al.* (LIGO Scientific, Virgo, Fermi GBM, INTEGRAL, IceCube, AstroSat Cadmium Zinc Telluride Imager Team, IPN, Insight-Hxmt, ANTARES, Swift, AGILE Team, 1M2H Team, Dark Energy Camera GW-EM, DES, DLT40, GRAWITA, Fermi-LAT, ATCA,

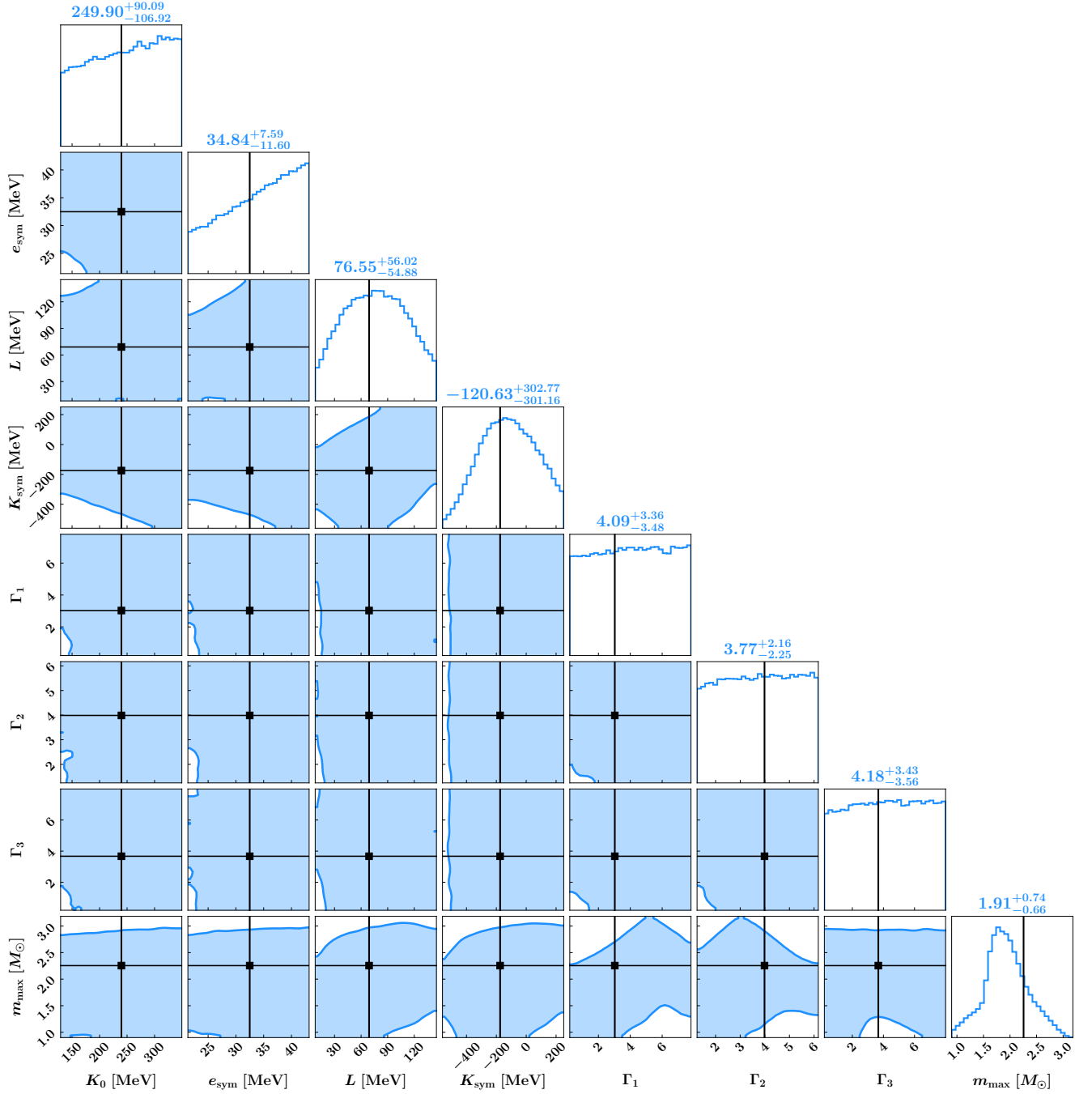


FIG. 14. Effective priors for the EoS parameters after imposing the causality constraint. The black solid lines represent the injected NS EoS parameters.

ASKAP, Las Cumbres Observatory Group, OzGrav, DWF (Deeper Wider Faster Program), AST3, CAAS-TRO, VINROUGE, MASTER, J-GEM, GROWTH, JAGWAR, CaltechNRAO, TTU-NRAO, NuSTAR, Pan-STARRS, MAXI Team, TZAC Consortium, KU, Nordic Optical Telescope, ePESSTO, GROND, Texas Tech University, SALT Group, TOROS, BOOTES, MWA, CALET, IKI-GW Follow-up, H.E.S.S., LOFAR, LWA, HAWC, Pierre Auger, ALMA, Euro VLBI Team, Pi of Sky, Chandra Team at McGill University, DFN, AT-

LAS Telescopes, High Time Resolution Universe Survey, RIMAS, RATIR, SKA South Africa/MeerKAT), “Multi-messenger Observations of a Binary Neutron Star Merger,” *Astrophys. J. Lett.* **848**, L12 (2017), arXiv:1710.05833 [astro-ph.HE].

- [7] B. P. Abbott *et al.* (LIGO Scientific, Virgo, 1M2H, Dark Energy Camera GW-E, DES, DLT40, Las Cumbres Observatory, VINROUGE, MASTER), “A gravitational-wave standard siren measurement of the Hubble constant,” *Nature* **551**, 85–88 (2017), arXiv:1710.05835

- [astro-ph.CO].
- [8] R. Abbott *et al.* (LIGO Scientific, VIRGO, KAGRA), “GWTC-3: Compact Binary Coalescences Observed by LIGO and Virgo During the Second Part of the Third Observing Run,” (2021), arXiv:2111.03606 [gr-qc].
- [9] Bernard F. Schutz, “Determining the Hubble Constant from Gravitational Wave Observations,” *Nature* **323**, 310–311 (1986).
- [10] Walter Del Pozzo, “Inference of the cosmological parameters from gravitational waves: application to second generation interferometers,” *Phys. Rev. D* **86**, 043011 (2012), arXiv:1108.1317 [astro-ph.CO].
- [11] Rachel Gray *et al.*, “Cosmological inference using gravitational wave standard sirens: A mock data analysis,” *Phys. Rev. D* **101**, 122001 (2020), arXiv:1908.06050 [gr-qc].
- [12] M. Soares-Santos *et al.* (DES, LIGO Scientific, Virgo), “First Measurement of the Hubble Constant from a Dark Standard Siren using the Dark Energy Survey Galaxies and the LIGO/Virgo Binary–Black-hole Merger GW170814,” *Astrophys. J. Lett.* **876**, L7 (2019), arXiv:1901.01540 [astro-ph.CO].
- [13] Andreas Finke, Stefano Foffa, Francesco Iacovelli, Michele Maggiore, and Michele Mancarella, “Cosmology with LIGO/Virgo dark sirens: Hubble parameter and modified gravitational wave propagation,” *JCAP* **08**, 026 (2021), arXiv:2101.12660 [astro-ph.CO].
- [14] Rachel Gray, Chris Messenger, and John Veitch, “A pixelated approach to galaxy catalogue incompleteness: improving the dark siren measurement of the Hubble constant,” *Mon. Not. Roy. Astron. Soc.* **512**, 1127–1140 (2022), arXiv:2111.04629 [astro-ph.CO].
- [15] Zhi-Qiang You, Xing-Jiang Zhu, Gregory Ashton, Eric Thrane, and Zong-Hong Zhu, “Standard-siren cosmology using gravitational waves from binary black holes,” *Astrophys. J.* **908**, 215 (2021), arXiv:2004.00036 [astro-ph.CO].
- [16] S. Mastrogiovanni, K. Leyde, C. Karathanasis, E. Chassande-Mottin, D. A. Steer, J. Gair, A. Ghosh, R. Gray, S. Mukherjee, and S. Rinaldi, “On the importance of source population models for gravitational-wave cosmology,” *Phys. Rev. D* **104**, 062009 (2021), arXiv:2103.14663 [gr-qc].
- [17] R. Abbott *et al.* (LIGO Scientific, Virgo, KAGRA, VIRGO), “Constraints on the Cosmic Expansion History from GWTC-3,” *Astrophys. J.* **949**, 76 (2023), arXiv:2111.03604 [astro-ph.CO].
- [18] Simone Mastrogiovanni, Danny Laghi, Rachel Gray, Giada Caneva Santoro, Archisman Ghosh, Christos Karathanasis, Konstantin Leyde, Daniele A. Steer, Stephane Perries, and Gregoire Pierra, “Joint population and cosmological properties inference with gravitational waves standard sirens and galaxy surveys,” *Phys. Rev. D* **108**, 042002 (2023), arXiv:2305.10488 [astro-ph.CO].
- [19] Rachel Gray *et al.*, “Joint cosmological and gravitational-wave population inference using dark sirens and galaxy catalogues,” *JCAP* **12**, 023 (2023), arXiv:2308.02281 [astro-ph.CO].
- [20] Masamune Oguri, “Measuring the distance-redshift relation with the cross-correlation of gravitational wave standard sirens and galaxies,” *Phys. Rev. D* **93**, 083511 (2016), arXiv:1603.02356 [astro-ph.CO].
- [21] Sayantani Bera, Divya Rana, Surhud More, and Sukanta Bose, “Incompleteness Matters Not: Inference of H_0 from Binary Black Hole–Galaxy Cross-correlations,” *Astrophys. J.* **902**, 79 (2020), arXiv:2007.04271 [astro-ph.CO].
- [22] Suvodip Mukherjee, Benjamin D. Wandelt, and Joseph Silk, “Probing the theory of gravity with gravitational lensing of gravitational waves and galaxy surveys,” *Mon. Not. Roy. Astron. Soc.* **494**, 1956–1970 (2020), arXiv:1908.08951 [astro-ph.CO].
- [23] Suvodip Mukherjee, Benjamin D. Wandelt, Samaya M. Nissanke, and Alessandra Silvestri, “Accurate precision Cosmology with redshift unknown gravitational wave sources,” *Phys. Rev. D* **103**, 043520 (2021), arXiv:2007.02943 [astro-ph.CO].
- [24] Cristina Cigarran Diaz and Suvodip Mukherjee, “Mapping the cosmic expansion history from LIGO-Virgo-KAGRA in synergy with DESI and SPHEREx,” *Mon. Not. Roy. Astron. Soc.* **511**, 2782–2795 (2022), arXiv:2107.12787 [astro-ph.CO].
- [25] Suvodip Mukherjee, Alex Krolewski, Benjamin D. Wandelt, and Joseph Silk, “Cross-correlating dark sirens and galaxies: measurement of H_0 from GWTC-3 of LIGO-Virgo-KAGRA,” (2022), arXiv:2203.03643 [astro-ph.CO].
- [26] Tathagata Ghosh, Surhud More, Sayantani Bera, and Sukanta Bose, “Bayesian framework to infer the Hubble constant from cross-correlation of individual gravitational wave events with galaxies,” (2023), arXiv:2312.16305 [astro-ph.CO].
- [27] Stephen R. Taylor, Jonathan R. Gair, and Ilya Mandel, “Hubble without the Hubble: Cosmology using advanced gravitational-wave detectors alone,” *Phys. Rev. D* **85**, 023535 (2012), arXiv:1108.5161 [gr-qc].
- [28] Stephen R. Taylor and Jonathan R. Gair, “Cosmology with the lights off: standard sirens in the Einstein Telescope era,” *Phys. Rev. D* **86**, 023502 (2012), arXiv:1204.6739 [astro-ph.CO].
- [29] C. Messenger and J. Read, “Measuring a cosmological distance-redshift relationship using only gravitational wave observations of binary neutron star coalescences,” *Phys. Rev. Lett.* **108**, 091101 (2012), arXiv:1107.5725 [gr-qc].
- [30] Deep Chatterjee, Abhishek Hegade K R, Gilbert Holder, Daniel E. Holz, Scott Perkins, Kent Yagi, and Nicolás Yunes, “Cosmology with Love: Measuring the Hubble constant using neutron star universal relations,” *Phys. Rev. D* **104**, 083528 (2021), arXiv:2106.06589 [gr-qc].
- [31] Tathagata Ghosh, Bhaskar Biswas, and Sukanta Bose, “Simultaneous inference of neutron star equation of state and the Hubble constant with a population of merging neutron stars,” *Phys. Rev. D* **106**, 123529 (2022), arXiv:2203.11756 [astro-ph.CO].
- [32] Banafsheh Shiralilou, Geert Raaijmakers, Bastien Duboef, Samaya Nissanke, Francois Foucart, Tanja Hinderer, and Andrew R. Williamson, “Measuring the Hubble Constant with Dark Neutron Star–Black Hole Mergers,” *Astrophys. J.* **955**, 149 (2023), arXiv:2207.11792 [astro-ph.CO].
- [33] Arnab Dhani, Ssohrab Borhanian, Anuradha Gupta, and Bangalore Sathyaprakash, “Cosmography with bright and Love sirens,” (2022), arXiv:2212.13183 [gr-qc].
- [34] Daniel Wysocki, Richard O’Shaughnessy, Leslie Wade, and Jacob Lange, “Inferring the neutron star equation of state simultaneously with the population of merging neutron stars,” (2020), arXiv:2001.01747 [gr-qc].

- [35] Jacob Golomb and Colm Talbot, “Hierarchical Inference of Binary Neutron Star Mass Distribution and Equation of State with Gravitational Waves,” *Astrophys. J.* **926**, 79 (2022), arXiv:2106.15745 [astro-ph.HE].
- [36] Vaibhav Tiwari, “Estimation of the Sensitive Volume for Gravitational-wave Source Populations Using Weighted Monte Carlo Integration,” *Class. Quant. Grav.* **35**, 145009 (2018), arXiv:1712.00482 [astro-ph.HE].
- [37] Will M. Farr, “Accuracy Requirements for Empirically Measured Selection Functions,” *Research Notes of the American Astronomical Society* **3**, 66 (2019), arXiv:1904.10879 [astro-ph.IM].
- [38] Bhaskar Biswas, Prasanta Char, Rana Nandi, and Sukanta Bose, “Towards mitigation of apparent tension between nuclear physics and astrophysical observations by improved modeling of neutron star matter,” *Phys. Rev. D* **103**, 103015 (2021), arXiv:2008.01582 [astro-ph.HE].
- [39] Bhaskar Biswas, Rana Nandi, Prasanta Char, Sukanta Bose, and Nikolaos Stergioulas, “GW190814: on the properties of the secondary component of the binary,” *Mon. Not. Roy. Astron. Soc.* **505**, 1600–1606 (2021), arXiv:2010.02090 [astro-ph.HE].
- [40] Bhaskar Biswas, “Impact of PREX-II and Combined Radio/NICER/XMM-Newton’s Mass–radius Measurement of PSR J0740+6620 on the Dense-matter Equation of State,” *Astrophys. J.* **921**, 63 (2021), arXiv:2105.02886 [astro-ph.HE].
- [41] Rossella Gamba, Jocelyn S. Read, and Leslie E. Wade, “The impact of the crust equation of state on the analysis of GW170817,” *Class. Quant. Grav.* **37**, 025008 (2020), arXiv:1902.04616 [gr-qc].
- [42] Bhaskar Biswas, Rana Nandi, Prasanta Char, and Sukanta Bose, “Role of crustal physics in the tidal deformation of a neutron star,” *Phys. Rev. D* **100**, 044056 (2019), arXiv:1905.00678 [gr-qc].
- [43] Gordon Baym, Christopher Pethick, and Peter Sutherland, “The Ground State of Matter at High Densities: Equation of State and Stellar Models,” *Astrophys. J.* **170**, 299 (1971).
- [44] Wen-Jie Xie and Bao-An Li, “Bayesian Inference of High-density Nuclear Symmetry Energy from Radii of Canonical Neutron Stars,” *Astrophys. J.* **883**, 174 (2019), arXiv:1907.10741 [astro-ph.HE].
- [45] M. Oertel, M. Hempel, T. Klähn, and S. Typel, “Equations of state for supernovae and compact stars,” *Rev. Mod. Phys.* **89**, 015007 (2017), arXiv:1610.03361 [astro-ph.HE].
- [46] Jocelyn S. Read, Benjamin D. Lackey, Benjamin J. Owen, and John L. Friedman, “Constraints on a phenomenologically parameterized neutron-star equation of state,” *Phys. Rev. D* **79**, 124032 (2009), arXiv:0812.2163 [astro-ph].
- [47] Nicholas Farrow, Xing-Jiang Zhu, and Eric Thrane, “The mass distribution of Galactic double neutron stars,” *Astrophys. J.* **876**, 18 (2019), arXiv:1902.03300 [astro-ph.HE].
- [48] Chris L. Fryer, Krzysztof Belczynski, Grzegorz Wiktorowicz, Michal Dominik, Vicky Kalogera, and Daniel E. Holz, “Compact Remnant Mass Function: Dependence on the Explosion Mechanism and Metallicity,” *Astrophys. J.* **749**, 91 (2012), arXiv:1110.1726 [astro-ph.SR].
- [49] S. Woosley, Tuguldur Sukhbold, and H. T. Janka, “The Birth Function for Black Holes and Neutron Stars in Close Binaries,” *Astrophys. J.* **896**, 56 (2020), arXiv:2001.10492 [astro-ph.HE].
- [50] Feryal Özel, Dimitrios Psaltis, Ramesh Narayan, and Antonia Sierra Villarreal, “On the Mass Distribution and Birth Masses of Neutron Stars,” *Astrophys. J.* **757**, 55 (2012), arXiv:1201.1006 [astro-ph.HE].
- [51] Bülent Kiziltan, Athanasios Kottas, Maria De Yoreo, and Stephen E. Thorsett, “The Neutron Star Mass Distribution,” *Astrophys. J.* **778**, 66 (2013), arXiv:1309.6635 [astro-ph.SR].
- [52] Feryal Özel and Paulo Freire, “Masses, Radii, and the Equation of State of Neutron Stars,” *Ann. Rev. Astron. Astrophys.* **54**, 401–440 (2016), arXiv:1603.02698 [astro-ph.HE].
- [53] Justin Alsing, Hector O. Silva, and Emanuele Berti, “Evidence for a maximum mass cut-off in the neutron star mass distribution and constraints on the equation of state,” *Mon. Not. Roy. Astron. Soc.* **478**, 1377–1391 (2018), arXiv:1709.07889 [astro-ph.HE].
- [54] Dong-Sheng Shao, Shao-Peng Tang, Jin-Liang Jiang, and Yi-Zhong Fan, “Maximum mass cutoff in the neutron star mass distribution and the prospect of forming supramassive objects in the double neutron star mergers,” *Phys. Rev. D* **102**, 063006 (2020), arXiv:2009.04275 [astro-ph.HE].
- [55] R. Abbott *et al.* (KAGRA, VIRGO, LIGO Scientific), “Population of Merging Compact Binaries Inferred Using Gravitational Waves through GWTC-3,” *Phys. Rev. X* **13**, 011048 (2023), arXiv:2111.03634 [astro-ph.HE].
- [56] B. P. Abbott *et al.* (KAGRA, LIGO Scientific, Virgo, VIRGO), “Prospects for observing and localizing gravitational-wave transients with Advanced LIGO, Advanced Virgo and KAGRA,” *Living Rev. Rel.* **21**, 3 (2018), arXiv:1304.0670 [gr-qc].
- [57] B. P. Abbott *et al.* (LIGO Scientific, Virgo), “Properties of the binary neutron star merger GW170817,” *Phys. Rev. X* **9**, 011001 (2019), arXiv:1805.11579 [gr-qc].
- [58] Xing-Jiang Zhu and Gregory Ashton, “Characterizing Astrophysical Binary Neutron Stars with Gravitational Waves,” *Astrophys. J. Lett.* **902**, L12 (2020), arXiv:2007.08198 [astro-ph.HE].
- [59] Tim Dietrich, Anuradha Samajdar, Sebastian Khan, Nathan K. Johnson-McDaniel, Reetika Dudi, and Wolfgang Tichy, “Improving the NRTidal model for binary neutron star systems,” *Phys. Rev. D* **100**, 044003 (2019), arXiv:1905.06011 [gr-qc].
- [60] Joshua S. Speagle, “DYNESTY: a dynamic nested sampling package for estimating Bayesian posteriors and evidences,” *Mon. Not. Roy. Astron. Soc.* **493**, 3132–3158 (2020), arXiv:1904.02180 [astro-ph.IM].
- [61] Gregory Ashton, Moritz Hübner, Paul D. Lasky, Colm Talbot, Kendall Ackley, Sylvia Biscoveanu, Qi Chu, Atul Divakarla, Paul J. Easter, Boris Goncharov, and et al., “Bilby: A user-friendly bayesian inference library for gravitational-wave astronomy,” *The Astrophysical Journal Supplement Series* **241**, 27 (2019).
- [62] J. Buchner, A. Georgakakis, K. Nandra, L. Hsu, C. Rangel, M. Brightman, A. Merloni, M. Salvato, J. Donley, and D. Kocevski, “X-ray spectral modelling of the AGN obscuring region in the CDFS: Bayesian model selection and catalogue,” *Astron. Astrophys.* **564**, A125

- (2014), arXiv:1402.0004 [astro-ph.HE].
- [63] Richard C. Tolman, “Static solutions of einstein’s field equations for spheres of fluid,” *Phys. Rev.* **55**, 364–373 (1939).
- [64] J. R. Oppenheimer and G. M. Volkoff, “On massive neutron cores,” *Phys. Rev.* **55**, 374–381 (1939).
- [65] Bhaskar Biswas and Stephan Rosswog, “Simultaneously constraining the neutron star equation of state and mass distribution through multimessenger observations and nuclear benchmarks,” in preparation (2024).
- [66] D. Adhikari *et al.* (PREX), “An Accurate Determination of the Neutron Skin Thickness of ^{208}Pb through Parity-Violation in Electron Scattering,” (2021), arXiv:2102.10767 [nucl-ex].
- [67] D. Adhikari *et al.* (CREX), “Precision Determination of the Neutral Weak Form Factor of Ca48,” *Phys. Rev. Lett.* **129**, 042501 (2022), arXiv:2205.11593 [nucl-ex].
- [68] C. Drischler, J. A. Melendez, R. J. Furnstahl, and D. R. Phillips, “Quantifying uncertainties and correlations in the nuclear-matter equation of state,” *Phys. Rev. C* **102**, 054315 (2020), arXiv:2004.07805 [nucl-th].
- [69] Praveer Tiwari, Dake Zhou, Bhaskar Biswas, Michael McNeil Forbes, and Sukanta Bose, “Framework for Multi-messenger Inference from Neutron Stars: Combining Nuclear Theory Priors,” (2023), arXiv:2306.04386 [astro-ph.HE].
- [70] Thomas E. Riley *et al.*, “A NICER View of PSR J0030+0451: Millisecond Pulsar Parameter Estimation,” *Astrophys. J. Lett.* **887**, L21 (2019), arXiv:1912.05702 [astro-ph.HE].
- [71] M. C. Miller *et al.*, “PSR J0030+0451 Mass and Radius from NICER Data and Implications for the Properties of Neutron Star Matter,” *Astrophys. J. Lett.* **887**, L24 (2019), arXiv:1912.05705 [astro-ph.HE].
- [72] Thomas E. Riley *et al.*, “A NICER View of the Massive Pulsar PSR J0740+6620 Informed by Radio Timing and XMM-Newton Spectroscopy,” *Astrophys. J. Lett.* **918**, L27 (2021), arXiv:2105.06980 [astro-ph.HE].
- [73] M. C. Miller *et al.*, “The Radius of PSR J0740+6620 from NICER and XMM-Newton Data,” *Astrophys. J. Lett.* **918**, L28 (2021), arXiv:2105.06979 [astro-ph.HE].
- [74] E. Fonseca *et al.*, “Refined Mass and Geometric Measurements of the High-mass PSR J0740+6620,” *Astrophys. J. Lett.* **915**, L12 (2021), arXiv:2104.00880 [astro-ph.HE].
- [75] Sylvia Biscoveanu, Colm Talbot, and Salvatore Vitale, “The effect of spin mismodelling on gravitational-wave measurements of the binary neutron star mass distribution,” *Mon. Not. Roy. Astron. Soc.* **511**, 4350–4359 (2022), arXiv:2111.13619 [astro-ph.HE].
- [76] T. Akutsu *et al.* (KAGRA), “Overview of KAGRA: Calibration, detector characterization, physical environmental monitors, and the geophysics interferometer,” *PTEP* **2021**, 05A102 (2021), arXiv:2009.09305 [gr-qc].
- [77] M. Saleem *et al.*, “The science case for LIGO-India,” *Class. Quant. Grav.* **39**, 025004 (2022), arXiv:2105.01716 [gr-qc].
- [78] Samantha A. Usman, Joseph C. Mills, and Stephen Fairhurst, “Constraining the Inclinations of Binary Mergers from Gravitational-wave Observations,” *Astrophys. J.* **877**, 82 (2019), arXiv:1809.10727 [gr-qc].
- [79] Matthew Evans *et al.*, “A Horizon Study for Cosmic Explorer: Science, Observatories, and Community,” (2021), arXiv:2109.09882 [astro-ph.IM].
- [80] Michele Maggiore *et al.*, “Science Case for the Einstein Telescope,” *JCAP* **03**, 050 (2020), arXiv:1912.02622 [astro-ph.CO].
- [81] Marica Branchesi *et al.*, “Science with the Einstein Telescope: a comparison of different designs,” *JCAP* **07**, 068 (2023), arXiv:2303.15923 [gr-qc].
- [82] Charlie T. Mpetha, Giuseppe Congedo, and Andy Taylor, “Future prospects on testing extensions to Λ CDM through the weak lensing of gravitational waves,” *Phys. Rev. D* **107**, 103518 (2023), arXiv:2208.05959 [astro-ph.CO].
- [83] R. Laureijs *et al.*, “Euclid Definition Study Report,” (2011), arXiv:1110.3193 [astro-ph.CO].
- [84] Sofia Canevarolo, Loek van Vonderen, and Nora Elisa Chisari, “Impact of lensing of gravitational waves on the observed distribution of neutron star masses,” (2024), arXiv:2404.11480 [astro-ph.CO].
- [85] Tanja Hinderer, “Tidal Love numbers of neutron stars,” *Astrophys. J.* **677**, 1216–1220 (2008), arXiv:0711.2420 [astro-ph].
- [86] Taylor Binnington and Eric Poisson, “Relativistic theory of tidal Love numbers,” *Phys. Rev. D* **80**, 084018 (2009), arXiv:0906.1366 [gr-qc].
- [87] Thibault Damour and Alessandro Nagar, “Relativistic tidal properties of neutron stars,” *Phys. Rev. D* **80**, 084035 (2009), arXiv:0906.0096 [gr-qc].